MYCN recruits the nuclear exosome complex to RNA polymerase II to prevent transcription-replication conflicts

Citation: Papadopoulos, Dimitrios, Solvie, Daniel, Baluapuri, Apoorva, Endres, Theresa, Ha, Stefanie Anh et al. 2022. "MYCN recruits the nuclear exosome complex to RNA polymerase II to prevent transcription-replication conflicts." Molecular Cell, 82 (1).

As Published: 10.1016/J.MOLCEL.2021.11.002

Publisher: Elsevier BV

Persistent URL: https://hdl.handle.net/1721.1/147120

Version: Author's final manuscript: final author's manuscript post peer review, without publisher's formatting or copy editing

MYCN recruits the nuclear exosome complex to RNA polymerase II to prevent transcription-replication conflicts

Dimitrios Papadopoulos[1], Daniel Solvie[1], Apoorva Baluapuri[2], Theresa Endres[1], Stefanie Anh Ha[1], Steffi Herold[1], Jacqueline Kalb[1], Celeste Giansanti[3], Christina Schülein-Völk[4], Carsten Patrick Ade[1], Cornelius Schneider[5], Abdallah Gaballa[1], Seychelle Vos[6], Utz Fischer[5], Matthias Dobbelstein[3], Elmar Wolf[2], and Martin Eilers[1,7*]

[1] Theodor Boveri Institute, Department of Biochemistry and Molecular Biology, Biocenter, University of Würzburg, Am Hubland, 97074 Würzburg, Germany

[2] Cancer Systems Biology Group, Department of Biochemistry and Molecular Biology, Biocenter, University of Würzburg, Am Hubland, 97074 Würzburg, Germany

[3] Institute of Molecular Oncology, Center of Molecular Biosciences, University of Göttingen, Justus von Liebig Weg 11, 37077 Göttingen, Germany

[4] Core Unit High-Content Microscopy, Biocenter, University of Würzburg, Am Hubland, 97074 Würzburg, Germany

[5] Department of Biochemistry, Biocenter, University of Würzburg, Am Hubland, 97074 Würzburg, Germany

[6] Massachusetts Institute of Technology, Department of Biology, 31 Ames Street, Cambridge, USA

[7] Lead contact; *Correspondence: martin.eilers@biozentrum.uni-wuerzburg.de

SUMMARY

The MYCN oncoprotein drives the development of numerous neuroendocrine and pediatric tumors. Here we show that MYCN interacts with the nuclear RNA exosome, a 3'-5' exoribonuclease complex, and recruits the exosome to its target genes. In the absence of the exosome, MYCN-directed elongation by RNA Polymerase II (RNAPII) is slow and non-productive on a large group of cell cycle-regulated genes. During the S-phase of MYCN-driven tumor cells, the exosome is required to prevent the accumulation of stalled replication forks and of double-strand breaks close to the transcription start sites. Upon depletion of the exosome, activation of ATM causes recruitment of BRCA1, which stabilizes nuclear mRNA decapping complexes, leading to MYCN-dependent transcription termination. Disruption of mRNA decapping in turn activates ATR, indicating transcription-replication conflicts. We propose that exosome recruitment by MYCN maintains productive transcription elongation during S-phase and prevents transcription-replication conflicts to maintain the rapid proliferation of neuroendocrine tumor cells.

INTRODUCTION

Deregulated expression of one of the three members of the *MYC* gene family is a major driver of tumorigenesis in numerous entities (Dang, 2012; Kress et al., 2015). The MYCN paralogue is physiologically expressed in rapidly proliferating neuronal cells early in development. In many pediatric and adult neuroendocrine tumors its expression is deregulated either due to genomic alterations at the MYCN locus or due to it being downstream of major oncogenic signaling pathways (Rickman et al., 2018). A paradigmatic example are *MYCN* amplifications in neuroblastoma patients, which drive the development of a subgroup with very poor prognosis (Brady et al., 2020).

Oncoproteins of the MYC family bind to virtually all active promoters and many enhancers and exert widespread effects on RNA Polymerase II (RNAPII) (Baluapuri et al., 2020; Kress *et al.*, 2015; Lourenco et al., 2021). MYC and MYCN proteins can stimulate several steps in the assembly of an elongation-competent RNAPII complex, with the effects on promoter clearance and elongation being predominant (Baluapuri et al., 2019; Buchel et al., 2017; de Pretis et al., 2017; Kalkat et al., 2018; Rahl et al., 2010; Walz et al., 2014). While MYCN promotes a global release of RNAPII from active promoters, RNAPII enters productive elongation only on a fraction of genes in response to MYCN activation and terminates at a promoter-proximal position on many genes (Herold et al., 2019). One mechanism by which MYCN promotes termination involves the recruitment of BRCA1, which stabilizes mRNA decapping complexes at MYCN-bound promoters (Herold *et al.*, 2019). Decapping of mRNA in turn initiates promoter-proximal transcription termination by the XRN2 5'-3´exonuclease (Brannan et al., 2012). Recruitment of BRCA1 by MYCN suppresses the accumulation of promoter-proximal R-loops, consistent with its functions in mammary carcinoma (Zhang et al., 2017) and Ewing sarcoma (Gorthi et al., 2018). How the dual control of transcription elongation and termination contributes to the oncogenic functions of MYCN is unknown.

During S-phase, conflicts between transcription and DNA replication can arise, which threaten genomic stability (Garcia-Muse and Aguilera, 2016; Hamperl and Cimprich, 2016). Origins of DNA replication are preferentially located close to transcription start sites, hence conflicts

between RNAPII and DNA polymerase complexes occur frequently at actively transcribed genes (Bayona-Feliu et al., 2021; Macheret and Halazonetis, 2018; Petryk et al., 2016). In eukaryotic cells, the PAF1 elongation factor can prevent conflicts of RNAPII with the replication fork (Poli et al., 2016). Both MYC and MYCN bind to PAF1c and MYC recruits PAF1c to RNAPII to repair transcription-induced double-strand breaks during S-phase (Buchel *et al.*, 2017; Endres et al., 2021; Jaenicke et al., 2016). Furthermore, MYCN recruits the Aurora-A kinase during S-phase; Aurora-A phosphorylates S10 on histone H.3.3, which prevents R-loop formation ahead of the replication fork (Roeschert et al., 2021). These observations suggest that MYC and MYCN proteins may prevent transcription-replication conflicts in rapidly proliferating tumor cells.

RNAPII frequently stalls during transcription, for example when RNAPII encounters obstacles to elongation, such as DNA damage, supercoiling, conflicts with the replication fork or AT-rich stretches in the DNA template (Ma et al., 2019; Noe Gonzalez et al., 2020; Sheridan et al., 2019; Zatreanu et al., 2019). Stalling can cause backtracking of RNAPII, which exposes the 3'-end of the nascent mRNA; this is a substrate for a nuclear 3'-5' exonuclease complex termed the exosome (Noe Gonzalez *et al.*, 2020). Stalling and backtracking of RNAPII also occur in response to increased supercoiling of DNA (Ma et al., 2013; Ma *et al.*, 2019). We show here that MYCN engages the nuclear RNA exosome to prevent conflicts between the DNA replication fork and RNAPII in MYCN-driven neuroblastoma cells.

RESULTS

Nuclear RNA exosome function is critical for MYCN-driven proliferation

We have previously found that BRCA1 is required for MYCN function using SH-EP-MYCNER neuroblastoma cells (Herold *et al.*, 2019). SH-EP cells express endogenous (c-)MYC; activation of a MYCNER chimera by addition of 4-hydroxytamoxifen (4-OHT) suppresses expression of endogenous MYC, leading to a switch from MYC to MYCN expression. To define the role of transcription termination in MYCN biology, we infected SH-EP-MYCNER cells with a doxycycline-inducible lentiviral library that targets 105 genes that encode proteins involved in transcription termination (Figure 1A). Also included were 55 shRNAs targeting housekeeping genes as well as control shRNAs targeting luciferase and GFP. The library was transduced at a low multiplicity of infection in triplicate samples and cells grew in the presence and absence of 4-OHT and in the presence and absence of doxycycline for a total of 10 doublings before isolation of genomic DNA. We ensured a 1000-fold representation of each shRNA at all times during cell culture (Figure 1A). Analysis of the resulting samples showed that the frequency and distribution of shRNAs was highly correlated amongst replicates (Figure S1A; Tables S1,2).

A waterfall plot of MYCN-dependent changes upon induction of the shRNA library showed that the abundance of control shRNAs that target either luciferase or GFP was not affected by MYCN activation (Figure 1B). In contrast, the screen identified a series of shRNAs that were strongly depleted in the presence of active MYCN (4-OHT); this included BRCA1, confirming our previous results (Figure 1B). Also, the screen identified the members of the mRNA decapping complex, DCP1A, DCP2, and EDC4, consistent with the finding that BRCA1 promotes chromatin association of DCP1A after MYCN activation (Herold *et al.*, 2019). Controls confirmed that none of the shRNAs were selected against in the absence of doxycycline and that different shRNAs targeting the same gene showed highly correlated changes in representation, confirming the on-target activity of the shRNAs (Table S1). The screen identified multiple shRNAs targeting splicing and polyadenyation factors, consistent with previous demonstrations that both processes are intimately linked to MYC function and

may constitute targetable vulnerabilities of MYCN driven tumors (Chiu et al., 2018; Fisher, 2020). Surprisingly, shRNAs targeting ten of the eleven subunits of the nuclear RNA exosome, a large 3'-5' exoribonucleolytic complex that can degrade nascent mRNA (Lingaraju et al., 2019), were also specifically depleted in the presence of active MYCN. In contrast, shRNAs targeting several of the proteins that target the exosome to specific substrates, such as ZCCHC8 and RBM7 that target it to non-spliced mRNAs (Lubas et al., 2011), were not depleted in the presence of MYCN (Figure 1B). Nuclear RNA exosome function has not previously been linked to MYCN biology, prompting us to investigate the functional relevance of this observation.

Validation experiments confirmed that an approximately 80% reduction in the amount of EXOSC10 subunit of the RNA exosome was well tolerated in control cells, but suppressed colony growth of SH-EP-MYCNER cells in the presence of 4-OHT correlating with a strong increase in apoptosis (Figures 1C,D; Figure S1B). EXOSC10 is one of the catalytic subunits of the nuclear RNA exosome and uses a conserved EFAVDLEHHS motif for degradation of RNA (Januszyk et al., 2011). Quantitative PCR (qPCR) assays confirmed that ectopic expression of a catalytically inactive allele of EXOSC10, that carries D313A and E315A mutations in the above motif, increased the amount of promoter upstream transcripts (PROMPTs), consistent with published data that the RNA exosome degrades PROMPTs (Figure 1E, Table S3) (Davidson et al., 2019). Expression of the D313A/E315A mutant allele of EXOSC10 suppressed colony formation of SH-EP-MYCNER cells in the presence of 4-OHT, but less so in the absence of 4-OHT, whereas expression of wildtype EXOSC10 was well tolerated (Figure 1F). Consistent with these observations, depletion of EXOSC10 suppressed colony formation and induced apoptosis of *MYCN*-amplified neuroblastoma cell lines, but had little effect on the growth of non-*MYCN* amplified neuroblastoma cells (Figure 1G, Figure S1C). We concluded that MYCN-expressing neuroblastoma cells depend on the nuclear exosome to escape apoptosis. Notably, inspection of available databases did not reveal consistent differences in expression of individual subunits of the RNA exosome between *MYCN*-amplified and non-*MYCN* amplified neuroblastoma tumors (Figure S1D).

MYCN recruits the RNA exosome to its target promoters

To determine whether MYCN forms complexes with the RNA exosome in cells, we initially performed transient transfection experiments, which showed that ectopically expressed HA-tagged MYCN associates with endogenous RNA exosome complexes (Figure S2A). To test whether endogenous MYCN forms complexes with the RNA exosome in cells, we immunoprecipitated MYCN and EXOSC10 from IMR-5 neuroblastoma cells that carry an amplified *MYCN* gene. EXOSC10 was present in α-MYCN, but not in control immunoprecipitates and conversely, MYCN was present in α-EXOSC10 immunoprecipitates (Figure 2A). This is consistent with our previous proteomic data (Buchel *et al.*, 2017). Notably, immunoprecipitations were performed after digestion of both RNA and DNA in cell lysates with benzonase and the interaction of both proteins was not disrupted by the addition of ethidium bromide to all buffers, demonstrating that the interaction is not mediated by DNA or RNA (Figure 2A). Virtually identical results were obtained using antibodies directed against EXOSC3 and DIS3, two additional subunits of the RNA exosome (Figure 2B). Incubation of a purified protein that contained the amino-terminal transcription regulatory domain of MYCN (amino acids 1-154) fused to maltose-binding protein (MBP) with HeLa nuclear protein extracts, showed that both EXOSC10 and EXOSC3, as well as RNAPII, were recovered in eluates from the MYCN-MBP-coupled amylose resin, but not from a control resin containing equal amounts of MBP, demonstrating that MYCN interacts with the exosome *in vitro* (Figures 2C,D).

In *Drosophila*, the nuclear exosome associates with active RNA Polymerase (Andrulis et al., 2002). Consistent with these observations, both the α-MYCN immunoprecipitates and those of EXOSC10 and EXOSC3 also contained RNAPII and were enriched for phosphorylated (RNAPII0) relative to unphosphorylated RNAPII (RNAPIIA), arguing that MYCN and the RNA exosome associate with active RNAPII (Figures 2A,B) (Phatnani and Greenleaf, 2006). This result was confirmed using antibodies that recognize RNAPII phosphorylated at Ser5 and Ser2 of the carboxy-terminal domain, which reflect promoter-bound paused and actively engaged RNAPII, respectively (Figure 2A). Proximity ligation assays (PLA) confirmed that EXOSC10

interacts with RNAPII and showed that activation of MYCN led to an increase in the interaction of EXOSC10 with pSer5 RNAPII, but not with unphosphorylated RNAPII or pSer2 RNAPII arguing that MYCN increases the interaction of both complexes at promoter-proximal sites before pause-release (Figure S2B). To test whether MYCN, RNAPII and the RNA exosome associate with each other, we fractionated nuclear protein extracts by glycerol gradient centrifugation and immunoprecipitated MYCN from pooled fractions of the gradient. Consistent with the notion that MYC proteins are present in several distinct protein complexes (Baluapuri *et al.*, 2019; Buchel *et al.*, 2017; Kalkat *et al.*, 2018), MYCN was broadly present in multiple high-molecular weight fractions in addition to the fractions expected for a dimeric MYCN/MAX complex (Figure 2E). Both EXOSC10 and EXOSC3 co-fractionated at fractions 12-17, which is compatible with the size of an intact RNA exosome (Macias et al., 2015) (Figure 2E). Notably, EXOSC10 co-immunoprecipitated with MYCN from fractions 15-17, which also contain RNAPII, but not from fractions 12-13, which do not contain RNAPII, although fractions 12-13 contain equal (MYCN, EXOSC10) or greater (EXOSC3) amount of both proteins than fractions 15-17 (Figure 2F).

Chromatin immunoprecipitation (ChIP) experiments showed that induction of MYCN recruits EXOSC10 to multiple MYCN-bound core promoters (Figure 2G). Notably, depletion of EXOSC10 had no detectable impact on MYCN chromatin binding (Figure S2C). MYCN also recruited EXOSC10 to the ACTB gene, although transcription of ACTB is not induced by MYCN, arguing that recruitment is not an indirect consequence of enhanced transcriptional activity (Figures S2D,E). To test whether endogenous MYCN is limiting for association of the exosome with RNAPII, we used shRNAs to deplete MYCN from *MYCN*-amplified IMR-5 neuroblastoma cells. Depletion of MYCN by about 70% decreased the association of EXOSC10 with total, pSer5, and pSer2 RNAPII, although the total amount of RNAPII and its phosphorylation status were unaffected by this level of MYCN depletion (Figure S2F,G). Taken together, we conclude that MYCN recruits the exosome to its target promoters and to RNAPII.

The RNA exosome has both MYCN-dependent and -independent effects on RNAPII

To explore how the RNA exosome affects MYCN-dependent control of RNAPII function, we depleted EXOSC10 using a doxycycline-inducible shRNA and activated MYCN by addition of 4-OHT before performing spike-in ChIP-sequencing (ChIP-RX) using antibodies against total RNAPII. Immunoblot controls established that MYCN had been activated since expression of endogenous MYC protein was repressed and that EXOSC10 was strongly depleted (Figure 3A). Notably, we did not detect global changes in the phosphorylation status of RNAPII under these conditions (Figure 3A).

Consistent with previous observations, inspection of individual genes showed that activation of MYCN globally increased chromatin association of total RNAPII (Figures 3B). Depletion of EXOSC10 strongly decreased chromatin association of RNAPII both under control conditions and upon activation of MYCN, which was observed both at individual genes and in density plots of genes longer than 8 kb; shorter genes were excluded from the analysis to match the 4sU-sequencing data discussed below (Figures 3B,C). Expression of the D313A/E315A mutant allele of EXOSC10 mimicked these effects, confirming that the nuclease activity of the exosome promotes RNAPII chromatin association during early transcription (Figure S3A). To further characterize the effects of EXOSC10 depletion, we performed ChIP-RX of pSer5 RNAPII and pSer2 RNAPII (Figure 3C). Average density plots of the region surrounding the transcription end site (TES) of all expressed genes showed that activation of MYCN also strongly increased chromatin association of pSer2 RNAPII with transcription end sites (Figure 3C). In contrast, MYCN decreased levels of pSer5 RNAPII downstream of the TSS (Figure 3C); both observations document a MYCN-dependent increase in transcription elongation and are consistent with multiple previous analyses of effects of MYC or MYCN on global RNAPII function (de Pretis *et al.*, 2017; Herold *et al.*, 2019; Rahl *et al.*, 2010; Walz *et al.*, 2014). Depletion of EXOSC10 decreased the association of total RNAPII and pSer5 RNAPII around the TSS in a MYCN-independent manner, arguing that the exosome promotes chromatin association of RNAPII. EXOSC10 depletion also reduced association of RNAPII and pSer2 RNAPII with the TES in the absence of MYCN; surprisingly, this decrease was not

observed when MYCN was activated (Figure 3C). This effect will be described in more detail together with the 4sU data in the next section (Figure 4).

EXOSC10 is a 3'-5' exoribonuclease, which can remove a 3' overhang of nascent mRNA from backtracked RNAPII to terminate transcription (Lemay et al., 2014). To resume transcription, stalling RNAPII requires a dedicated elongation factor, TFIIS (Noe Gonzalez *et al.*, 2020). To test how TFIIS functionally interacts with EXOSC10, we depleted TFIIS (Fish and Kane, 2002; Izban and Luse, 1992; Reines et al., 1989). TFIIS is encoded by three genes (*TCEA1-3*): in SH-EP cells, *TCEA1* exhibits the highest expression levels, while *TCEA2* and *TCEA3* are expressed weakly or not at all, respectively (Figure S3B). In contrast to the exosome, MYCN did not interact with TCEA1 in co-immunoprecipitation assays (Figure S3C) and ChIP assays showed that MYCN had no consistent effect on the association of TCEA1 with MYCN target promoters (Figure S3D). We used a doxycycline-inducible shRNA to deplete TCEA1, but noted that it also partially depletes TCEA2 (Figure 3D and Figure S3E). Consistent with a model in which TFIIS and the exosome exert competing effects on stalling RNAPII, depletion of TCEA1 enhanced the proximity of EXOSC10 with RNAPII (Figure S3F). ChIP-RX using antibodies against total RNAPII upon activation of MYCN in control and TCEA1-depleted cells showed that depletion of TCEA1 alone had little effect on chromatin association in control cells (Figures 3E,F and Figure S3G). Strikingly, MYCN activation in TCEA1-depleted cells led to a dramatic global decrease in chromatin association of RNAPII (Figures 3E,F and Figure S3G). Notably, activation of MYCN suppressed chromatin association of RNAPII both on genes that have been reported as MYCN-activated as well as on MYCN-repressed genes, further supporting the global nature of the effect (Figure S3G). Collectively, our data show first that the exosome enhances chromatin association of RNAPII in a MYCN-independent manner. Second, MYCN causes a widespread decrease in RNAPII chromatin association with chromatin in the absence of TFIIS. While this is not formally shown, these observations suggest that MYCN causes RNAPII to terminate in the absence of TFIIS; the enhanced proximity between RNAPII and the exosome upon TFIIS depletion suggests that the exosome contributes to termination.

The RNA exosome is required for MYCN-dependent transcription of cell cycle-regulated genes

To understand why depletion of EXOSC10 is synthetic lethal with MYCN activation, we asked whether RNAPII is functional if EXOSC10 is depleted in MYCN-activated cells. To do so, we pulse-labelled cells by addition of 4-thiouridine (4sU) and analyzed the effects of MYCN induction in control and EXOSC10-depleted cells immediately after a 20-minute pulse (Figure 4A). For the study of nascent transcription only intronic 4sU-seq reads were taken into consideration, therefore we restricted our analyses to expressed genes longer than 8 kb, as shorter genes exhibit a very low number of reads after filtering of exons and UTRs. In these experiments, we noted two effects of EXOSC10 depletion: first, depletion of EXOSC10 by itself caused an increase in nascent transcript accumulation: this is consistent with the observations cited above that the RNA exosome degrades PROMPTs and intron-containing other incorrectly processed transcripts (Davidson *et al.*, 2019). Importantly, while MYCN increased overall 4sU-labelled RNA synthesis in control cells, activation of MYCN in EXOSC10-depleted cells led to a decrease in overall 4sU-RNA synthesis (Figure 4A). Samples harvested from cells in which pulse-labelling of 4sU was followed by a 120-minute chase yielded results that are identical to the non-chased samples, demonstrating that the MYCN-induced decrease in 4sU-incorporation is due to inefficient transcription, not processing (Figure S4A). Notably, the decrease in 4sU-incorporation upon MYCN activation was not reflected in an overall decrease in association of pSer2 RNAPII with chromatin (shown for the TES in Figure 3C), arguing that the MYCN-driven elongation is slow and non-productive upon exosome depletion.

The change in 4sU-RNA levels upon exosome depletion in the response to MYCN was not uniform, but differed among genes (Figure 4B and Figure S4B). Specifically, at a cut-off of $p \leq 0.05$, transcription of 1516 genes was induced by MYCN in control cells, but either not induced or decreased by MYCN in EXOSC10-depleted cells (Figure 4B). PCR experiments using intronic primers validated these observations for individual genes (Figure 4C and Figure S4C; genes are indicated in Figure 4B). MYCN activation increased RNAPII occupancy around the TSS on this group of genes both in control and in EXOSC10-depleted cells, demonstrating that MYCN-dependent RNAPII loading onto these genes was not impaired by EXOSC10

depletion (Figures S4D). Together with the data shown in Figure 3C, the data argue that MYCN-driven elongation is non-productive for a specific group of genes in EXOSC10-depleted cells. Gene ontology (GO) enrichment analysis of nascent RNA synthesis demonstrated that this group of genes was highly enriched in genes that mediate progression through S- and G2-phases of the cell cycle (Figure 4D), suggesting that the MYCN-exosome interaction is required for cell cycle progression.

The RNA exosome prevents MYCN-driven double-strand break formation in S-phase

The specific effect on cell cycle-regulated genes was surprising, since PLAs showed that RNAPII is in proximity to both EXOSC10 and TCEA1 to a similar degree during all phases of the cell cycle (Figure S4E). Consistent with the effects on gene expression, depletion of EXOSC10 in MYCN-activated, but not in control cells, led to a significant increase in the percentage of cells in the G2-phase, suggesting that their passage into mitosis is retarded (Figure 4E). Determining the cell cycle distribution at several times after release from a double-thymidine block showed that EXOSC10 depletion also delayed progression of MYCN-driven cells through S-phase (Figure S4F). Since depletion of EXOSC10 in MYCN-driven cells both retarded passage through S- and G2-phase and induced apoptosis, we speculated that it might induce DNA damage. To explore this hypothesis, we labelled replicating cells with 5-ethynyl-2'-deoxyuridine (EdU), stained for γH2A.x and performed high-content microscopy analyses. Depletion of EXOSC10 led to an increase in the number of γH2A.x nuclear foci in the S- and the G2-phases and MYCN activation further elevated their number in both phases (Figures 4F,G and Figure S4G).

To better understand the DNA damage caused by EXOSC10-depletion in MYCN-driven cells, we probed immunoblots of cell lysates with antibodies directed against DNA damage markers. These experiments showed that activation of MYCN in EXOSC10-depleted cells induced phosphorylation of H2A.x, pKAP1 S824 and RPA32 S4/8, whereas depletion of EXOSC10 in control cells or activation of MYCN in wildtype cells had much smaller or no effects (Figure 5A). These sites are phosphorylated by the ATM kinase and DNA-PK, which monitor double-strand

breaks; furthermore, depletion of EXOSC10 moderately increased phosphorylation of CHK2 at T68 upon activation of MYCN, which is also targeted by ATM (Figure 5A and Figure S5A). In contrast, depletion of EXOSC10 by itself or in combination with activation of MYCN had no significant effect on phosphorylation of S345 of CHK1, a target site of the ATR kinase (Figure 5B). Depletion of another exosome subunit, EXOSC5, also led to a MYCN-dependent accumulation of phosphorylated KAP1, H2Ax and CHK2 (Figure S5B) and depletion of EXOSC10 also caused increased levels of pATM and pKAP1, but not pCHK1, in *MYCN*-amplified IMR-32 cells (Figure S5C). We concluded that the exosome is required to prevent activation of the ATM kinase in MYCN-driven tumor cells.

To determine whether double-strand break accumulate in a specific cell cycle phase, we arrested cells at the G1/S boundary by double-thymidine block and harvested cells at several time points after release from the block. This resulted in highly enriched G1-, S- and G2-phase cell populations (Figure S5D). Immunoblotting showed that pKAP1S824 was easily detectable in S-phase cells, while its levels were lower in G1- or G2-phase cells (Figures 5C,D). As control, we showed that incubation of cells with etoposide, a specific inhibitor of topoisomerase II that induces double-strand breaks, induced KAP1 phosphorylation in all phases of the cell cycle (Figure 5C). To understand this observation, we performed BLISS (Breaks Labeling *In Situ* and Sequencing), which allows genome-wide identification of double-strand breaks (Yan et al., 2017). The results showed that double-strand breaks accumulate after EXOSC10 depletion in MYCN-driven cells (Figure 5E,F). Notably, 2210/23778 breaks localized within 1.5 kb of the TSS of active genes and MYCN binding sites (see Figure 5F for a example). Since these promoter-proximal regions correspond to a small fraction of the entire genome, this suggested that double-strand breaks accumulate preferentially at TSS. To understand this observation, we performed ChIP-RX for FANCD2, which indicates the position of stalled replication forks (Bayona-Feliu *et al.*, 2021); control experiments confirmed that addition of aphidicolin, which inhibits ongoing DNA replication, strongly enhanced the signal (Figure S5E). The analysis showed that stalled forks were present close to MYCN binding sites at 866 promoters (Figure 5F and Figure S5F). The extent of fork stalling increased in response to

EXOSC10 depletion in MYCN-driven cells (Figure 5F and S5G) and a subset (323/866) of stalled forks were present in close vicinity of double-strand breaks (Figure S5F). Notably, comparison with a DRIPc-seq (Sanz and Chedin, 2019) dataset that mapped R-loops (Figure S5H) showed that R-loops were typically not detectable around the TSS and MYCN binding sites where double-strand breaks and FANCD2 accumulated after EXOSC10 depletion in MYCN-driven cells (see Figure S5I for an example). These observations suggest that double-strand breaks occur at least in part as consequence of unresolved transcription-replication conflicts. Consistent with this interpretation, PLAs showed that induction of MYCN in control cells decreased the overall proximity of PCNA, the sliding clamp that stabilizes replicative DNA polymerases with RNAPII; in contrast, depletion of EXOSC10 strongly enhanced the proximity of both proteins and activation of MYCN was unable to revert this effect in EXOSC10-depleted cells (Figure 5G). Furthermore, DNA fiber assays showed that MYCN activation in EXOSC10-depleted cells, but not in control cells, significantly slowed replication fork progression (Figures 5H,I). We concluded that the RNA exosome enables MYCN-driven tumor cells to prevent double-strand break accumulation in S-phase and escape transcription-replication conflicts.

ATM limits MYCN-dependent transcription elongation via BRCA1 and mRNA decapping

The observation that MYCN activation induces ATM activity in EXOSC10-depleted cells led us to wonder whether ATM activity shapes MYCN-dependent transcription. To address this question, we used 4sU-sequencing of newly synthesized mRNA and compared the responses to MYCN activation in the absence and presence of KU-60019, a specific inhibitor of the ATM kinase (Golding et al., 2009). Immunoblot controls confirmed that the inhibitor blocks etoposide-induced phosphorylation of CHK2 at T68 (Figure 6A). In these experiments, ATM inhibition had little effect on transcription in control cells (Figure 6B). However, when combined with MYCN activation, ATM inhibition strongly enhanced RNA synthesis on MYCN-activated genes and attenuated the MYCN-dependent decrease on repressed genes (Figure 6B). This effect was also apparent upon inspection of browser tracks of individual MYCN-activated and

-repressed genes (Figures 6C). To understand how ATM inhibition exerts this effect, we turned to our previous observation that MYCN recruits the BRCA1 protein to core promoters and that BRCA1 in turn recruits mRNA decapping complexes that can terminate transcription (Brannan *et al.*, 2012; Herold *et al.*, 2019). BRCA1 is recruited to double-strand breaks as part of the homology-directed repair machinery upon phosphorylation by the ATM kinase (Cortez et al., 1999; Venkitaraman, 2014). To test whether recruitment of BRCA1 depends on ATM, we activated MYCN in the presence or absence of KU-60019. ChIP assays using primers for a number of MYCN target genes showed that inhibition of ATM strongly attenuated recruitment of BRCA1 by MYCN, arguing that BRCA1 is recruited downstream of ATM (Figure 6D). BRCA1 associates with EDC4, a scaffold protein of the mRNA decapping complex, and promotes nuclear import of EDC4 (Hernandez et al., 2018). Proximity ligation assays showed that induction of MYCN enhanced the proximity between the decapping protein, DCP1A, and RNAPII in an BRCA1- and ATM-dependent manner (Figures 6E,F and Figure S6A). Collectively, the data show that activation of ATM recruits BRCA1 and, downstream of BRCA1, DCP1A to MYCN-bound promoters. To explore the functional consequence of DCP1A recruitment, we depleted DCP1A using a doxycycline-inducible shRNA and performed ChIP-RX using antibodies against total RNAPII and pSer2 RNAPII. Depletion of DCP1A alone had only minor effects on chromatin association of total RNAPII in control cells. Coupled with MYCN activation, depletion of DCP1A enhanced chromatin association of both total and pSer2 RNAPII on MYCN-activated genes and attenuated the decrease in their binding on MYCN-repressed genes (Figure 6G). Taken together, these observations show that MYCN-mediated termination depends, at least in part, on ATM activation and subsequently DCP1A function.

mRNA decapping prevents MYCN-dependent transcription-replication conflicts

To explore the physiological consequences of DCP1A depletion on MYCN-driven proliferation, we performed immunoblots of control and DCP1A-depleted cell lysates (Figure 7A). In contrast to EXOSC10 depletion, loss of DCP1A led to MYCN-dependent activation of ATR, as indicated

by an increase in phosphorylation of RPA32 S33 and of CHK1 S345, both target sites of ATR. In contrast, depletion of DCP1A, had little effect on phosphorylation of KAP1, an ATM target site, either in control or in MYCN-activated cells (Figure 7A). To understand when this damage occurs during the cell cycle, we labelled cells with EdU and stained for γH2A.x before analyzing them using quantitative immunofluorescence (Figures 7B,C). Activation of MYCN in DCP1A-depleted cells led to a strong increase in the number of γH2A.x-positive nuclei in the S-phase of the cell cycle (Figure 7B,C and Figure S6B). Furthermore, DNA fiber assays showed significantly shorter DNA fibers in DCP1A-depleted and MYCN-activated cells (Figures 7D,E). To investigate whether the inhibition of DNA replication correlates with an increase in transcription-replication conflicts, we performed PLAs with RNAPII and PCNA, or RAD1 and RAD9, which replace PCNA upon stalling of a replication fork. All three assays showed a significant increase in the number of foci when MYCN was activated in DCP1A-depleted cells, arguing that both active and stalled replication forks are in close proximity to RNAPII under these conditions (Figure 7F and Figure S6C,D). We concluded that abrogation of MYCN- and DCP1A-mediated termination leads to an increased incidence of collisions with replication forks and ATR activation. A model that summarizes our findings is shown in Figure 7G.

DISCUSSION

Here we show that MYCN interacts with and recruits the nuclear exosome to its target genes and that *MYCN*-amplified neuroblastoma cells depend on the exosome to maintain productive elongation and prevent excessive DNA damage. The nuclear exosome binds to nascent RNAs via its interaction with RNA-binding adaptor proteins (Kilchert et al., 2016; Zinder and Lima, 2017). Notably, MYCN-driven cells do not show an enhanced dependence on the targeting subunits ZCCH8 and RBM7 of the NEXT complex, which enables the exosome to degrade unspliced mRNAs (Lubas *et al.*, 2011), the ZC3H3 subunit of the PAXT complex (Silla et al., 2020), and MTREX, which is both part of NEXT and PAXT complexes, suggesting that the interaction of the exosome with MYCN has a separate function from these well-characterized complexes. This interpretation is consistent with the results of glycerol gradient centrifugation experiments, which indicate that MYCN is present in only a fraction of cellular exosome complexes.

In addition to its quality control function, exosome-mediated RNA degradation facilitates the resolution of R-loops (Richard et al., 2013) and promotes double-strand break repair (Domingo-Prim et al., 2019; Marin-Vicente et al., 2015). During transcription, the RNA exosome can degrade the extruding 3'-end of a nascent transcript still bound to a stalling and backtracked RNAPII (Lemay *et al.*, 2014; Proudfoot, 2016). The restart of stalling RNAPII depends on TFIIS, which induces RNAPII to endonucleolytically cleave nascent mRNA (Palangat et al., 2005; Reines *et al.*, 1989).

Consistent with its range of functions, ChIP- and 4sU-sequencing data show that the exosome has both MYCN-independent and MYCN-dependent roles in neuroblastoma cells. First, the RNA exosome maintains global chromatin occupancy of RNAPII independently of MYCN, likely by promoting a TFIIS-dependent restart of RNAPII that stalls during elongation. Second, the exosome assumes an additional function specifically in MYCN-driven tumor cells by maintaining productive transcription for a large group of genes required for progression through the S- and G2-phases of the cell cycle and preventing double-strand break accumulation and stalling of replication forks in MYCN-driven tumor cells. Depletion of the exosome causes the

accumulation of stalled forks and double-strand breaks near the TSS and to MYCN binding sites. We propose two possible mechanisms to explain this dependence: First, progressing replication forks generate a positive supercoil ahead of the fork and this torsional stress can induce stalling and backtracking of RNAPII, thereby enhancing the dependence on the exosome (Ma *et al.*, 2013; Ma *et al.*, 2019). Consequently MYCN-driven elongation is slow and non-productive in the absence of EXOSC10. Second, the MYCN-specific exosome function may be related to its function in homologous recombination (Domingo-Prim *et al.*, 2019). Similarly, MYCN recruits the BRCA1 protein, which is central to homologous recombination, to core promoters (Herold *et al.*, 2019; Venkitaraman, 2014). We show here that BRCA1 recruitment depends on an active ATM kinase, suggesting that it occurs in response to double-strand break formation. Collectively, our data argue that MYCN recruits the exosome, and, indirectly, BRCA1 to terminate transcription at promoters upon stalling of replication forks to prevent transcription-replication conflicts. Notably, both the dependency on the exosome and on BRCA1 are specific for *MYCN*-amplified neuroblastomas, arguing that MYC and MYCN differ in how they enable tumor cells to cope with replication stress and suggesting that these dependencies define tumor-specific vulnerabilities that can be exploited for therapy.

Depletion of EXOSC10 leads to activation of the ATM, but not ATR kinase. Notably, transcription-replication conflicts can be either co-directional or head-on; experiments using an episomal system show that co-directional conflicts activate the ATM kinase, while head-on conflicts activate ATR (Hamperl et al., 2017). Since origins of replication are close to transcription start sites, conflicts between the replication fork and RNAPII are often co-directional (Petryk *et al.*, 2016). Downstream of BRCA1, the mRNA decapping protein DCP1A is recruited, which restricts MYCN-driven transcription. Depletion of DCP1A activates ATR, suppresses DNA replication and enhances the proximity of RNAPII with stalled replication forks in a MYCN-dependent manner, suggesting that depletion of DCP1A causes head-on transcription-replication conflicts. The most likely interpretation of our data is, therefore, that recruitment of the exosome by MYCN is part of a two-tiered mechanism, which enables neuroblastoma to prevent fatal conflicts of DNA replication with RNAPII.

Limitations of the study

This conclusion underlies two limitations: First, while the subunits of the RNA exosome were clear hits in the shRNA screen, other factors were also consistently synthetic lethal with MYCN amplication, such as several splicing factors; the mechanism by which MYCN enables tumor cells to resolve transcription-replication conflicts may therefore involve additional mechanisms and factors. Second, the screen was performed in tissue culture, not *in vivo*. Since cells proliferate faster in culture than *in vivo*, the precise dependence of MYCN-driven tumor growth on the mechanisms that resolve transcription-replication conflicts remains to be determined.

ACKNOWLEDGMENTS

This work was supported by grants from the European Research council (AuroMYC), the European Regional Development (EFRE), German Cancer Aid (Enable), the Federal Ministry of Education and Research (DKTK), and the German Research Foundation via the DFG Research Group 2314 ("Targeting Therapeutic Windows in essential cellular processes for tumor therapy"). We thank Ryan Ramjan, Ulrike Samfass and Jürgen Ohmer for expert technical assistance, Matthias Fischer and Christoph Bartenhagen from the University Hospital Cologne for the neuroblastoma patient RNA-seq data.

AUTHOR CONTRIBUTIONS

Conceptualization, D.P. and M.E.; Methodology, D.P., J.K., D.S. and M.E.; Investigation, D.P., J.K., S.H., T.E., S.A.H., C.G., C.S.-V, A.G., and C.S.; Formal Analysis, D.S., A.B. and C.P.A.; Writing – Original Draft, D.P. and M.E.; Funding Acquisition, M.E.; Supervision, U.F., M.D. and M.E.

DECLARATION OF INTERESTS

The authors declare no competing interests.

FIGURE LEGENDS

Figure 1. Nuclear RNA exosome function is critical for MYCN-driven proliferation.

(A) Experimental outline of pooled shRNA screen in SH-EP-MYCNER cells using doxycycline (Dox)-inducible shRNAs (M.O.I.: multiplicity of infection; in all legends EtOH: ethanol, 4-OHT: 4-hydroxytamoxifen (100 nM unless indicated otherwise), Dox: Doxycycline (1 µg/ml)).

(B) Waterfall plot showing the median log_2 fold change (FC) in shRNA representation for each gene between Dox and Dox/4-OHT conditions (n=6; in all legends, n indicates the number of independent biological replicates).

(C) (Left) Immunoblot of SH-EP-MYCNER cells stably expressing Dox-inducible shRNAs targeting EXOSC10 after 72 h of Dox treatment. Beta actin (ACTB) was used as loading control (n=3). (Right) Clonogenic assay of SH-EP-MYCNER cells stably expressing EXOSC10 or luciferase shRNA after 120 h incubation with Dox and 4-OHT, as indicated (n=3 for luciferase and shEXOSC10 #2, n=1 for shEXOSC10 #1).

(D) Annexin V/propidium iodide FACS analysis of SH-EP-MYCNER cells stably expressing Dox-inducible EXOSC10 shRNA after 120 h of Dox and 4-OHT incubation, as indicated. Dots indicate biological replicates (n=3; in all subsequent panels, shEXOSC10 denotes EXOSC10 depletion by Dox addition).

(E) qPCR of the indicated promoter upstream transcripts (PROMPTs) in SH-EP-MYCNER cells expressing either a Dox-inducible EXOSC10 shRNA (72 h Dox incubation) or constitutively expressing EXOSC10 D313A/E315A inactive mutant. Dots indicate biological replicates (n=2).

(F) Clonogenic assay in SH-EP-MYCNER cells expressing either wild-type EXOSC10 or EXOSC10 D313A/E315A mutant (n=2).

(G) (Left) Immunoblots of a panel of *MYCN* amplified and non-*MYCN* amplified neuroblastoma cell lines stably expressing a Dox-inducible EXOSC10 shRNA after 72 h of Dox treatment (shEXOSC10). Vinculin (VCL) was used as loading control (n=2). Numbers indicated relative levels of EXOSC10. (Right) Clonogenic assay of the same cell lines after 120 h incubation with Dox (n=3).

Figure 2. MYCN recruits the RNA exosome to its target promoters.

(A) Immunoblot of MYCN and EXOSC10 immunoprecipitations (IP) from IMR-5 cells. All samples were treated with 50 U/ml benzonase before precipitations and ethidium bromide (EtBr;1 µg/ml) was present in all buffers, where indicated. Beta actin (ACTB) was used as loading control (n=3).

(B) Immunoblot of endogenous EXOSC3 and DIS3 IPs from IMR-5 cells. Samples were treated as above. ACTB was loading control. The asterisk (*) denotes the antibody heavy chain and the dagger (†) denotes an unspecific band (n=3 for EXOSC3, n=2 for DIS3).

(C) Coomassie Blue staining of purified His_6-MBP (MBP) and His_6-MBP-TEV-$MYCN^{1-154}$ (MBP-$MYCN^{1-154}$) (n=2).

(D) Immunoblot of pull-down experiment using HeLa nuclear protein lysate and purified MBP or MBP-$MYCN^{1-154}$ constructs. Eluate fractions correspond to proteins pulled-down by the indicated construct and supernatant fractions were collected after coupling but before washing and elution steps. Histone H3 was used as loading control (n=3).

(E) Immunoblot of endogenous RNAPII, MYCN, EXOSC10, and EXOSC3 sedimentation patterns in 10 %-30 % glycerol gradients from IMR-5 nuclear protein extracts. Extracts were treated with 50 U/ml benzonase. The asterisks (*) denote unspecific bands (n=3).

(F) Immunoblot of MYCN IP using pooled glycerol gradient fractions of IMR-5 nuclear protein extracts (n=4).

(G) ChIP-qPCR showing EXOSC10 binding to indicated loci in SH-EP-MYCNER cells. All primers used are proximal to the transcription start site. Cells were treated for 4 h with 4-OHT (200 nM), where indicated. Dots indicate technical replicates (n=2).

Figure 3. The RNA exosome has both MYCN-dependent and -independent effects on RNAPII.

(A) Immunoblot of SH-EP-MYCNER Dox-inducible EXOSC10 shRNA cells. Cells were treated for 72 h with Dox (shEXOSC10) and then for 4 h with 4-OHT (200 nM) where indicated. Beta actin (ACTB) was used as loading control (n=2).

(B) Genome browser tracks from spike-in ChIP-sequencing (ChIP-RX) of total RNAPII chromatin binding on *PTMA* locus. Same cells and conditions are as in panel (A) (n=2).

(C) Trimmed (1 %) mean read density of total, pSer5 and pSer2 RNAPII ChIP-RX data for all expressed genes, longer than 8 kb. Plots are centered around the TSS for total and pSer5 RNAPII (left) or TES for total and pSer2 RNAPII (right). The heatmaps above each plot indicate the p-value of the 4-OHT/EtOH difference in the presence of Dox, calculated from the density values of individual genes at each genomic location (RPM, reads per million; TSS, transcription start site; TES, transcription end site) (n=2).

(D) Immunoblot of SH-EP-MYCNER cells expressing a Dox-inducible shRNA against TCEA1. Cells were treated with Dox for 72 h (shTCEA1) and for 4 h with 4-OHT (200 nM) where indicated. Vinculin (VCL) was loading control (n=2).

(E) Genome browser tracks from ChIP-RX of total RNAPII chromatin binding on *NPM1* locus. Experimental conditions are as in panel (D) (n=2).

(F) Trimmed (1 %) mean read density of total RNAPII ChIP-RX data for expressed genes (>8 kb). Plots are either centered around the TSS (left) or TES (right) (n=2).

Figure 4. The RNA exosome is required for MYCN-dependent transcription of cell cycle-regulated genes.

(A) Trimmed (1 %) mean read metagene plot of 4sU-seq data in SH-EP-MYCNER cells expressing Dox-inducible EXOSC10 shRNA; genes longer than 8 kb are shown. Cells were treated for 72 h with Dox (shEXOSC10) and for 4 h with 4-OHT (200 nM) where indicated, and 4sU (500 μM) was added during the last 20 min of culture. RNA was harvested immediately after the 4sU pulse. The heatmap above the plot indicates the p-value of the 4-OHT/EtOH difference in the presence of Dox, calculated from the density values of individual genes at each genomic location. Shown are merged replicates (n=2).

(B) Volcano plot showing $\log_2$ fold changes (x-axis) and the statistical significance (y-axis) of 4sU-labelled RNA levels between control (EtOH) and Dox (shEXOSC10) conditions in the presence of 4-OHT. Cells were treated with Dox for 72 h (shEXOSC10) and then for 4 h with

4-OHT (200 nM) where indicated, and 4sU (500 μM) was added during the last 20 min of culture. RNA was harvested after a 120 min chase. A p-value cut-off of 0.05 was applied to count significantly altered genes. Genes used for subsequent validation are indicated (n=3).

(C) (Top) Genome browser tracks showing 4sU-RNA levels at loci indicated in panel (B). (Bottom) qPCR validation of RNA levels depicted in the above browser tracks. Experimental conditions as in panel (B). The PCR-amplified regions are represented by vertical lines below each browser track. Dots indicate biological replicates (n=3).

(D) GO Term enrichment analysis of the genes with a significant negative log_2FC (n=1516) indicated in panel (B).

(E) Cell cycle distribution of EdU-pulsed SH-EP-MYCNER cells expressing Dox-inducible EXOSC10 shRNA. Cells were treated for 96 h with Dox (shEXOSC10) and 4-OHT, as indicated. EdU (10 μM) pulse took place in the last 30 min of culture. Cell cycle phase distribution analysis was based on EdU and Hoechst stainings (n=9).

(F) Two-dimensional diagrams showing nuclear γH2A.x foci relative to EdU incorporation (y-axis) and DNA content (Hoechst staining; x-axis). Experimental conditions are as in (E) (n=3).

(G) Quantification and cell cycle distribution of nuclear γH2A.x foci, derived from panel (F) (n=3).

Figure 5. The RNA exosome prevents MYCN-driven double-strand break formation in S-phase.

(A) and (B) Immunoblots of SH-EP-MYCNER Dox-inducible EXOSC10 shRNA cells. Cells were treated for 96 h with Dox (shEXOSC10) and 4-OHT, as indicated. ACTB or VCL were used as loading controls. The asterisks (*) denote unspecific bands (n=3).

(C) Immunoblot of SH-EP-MYCNER Dox-inducible EXOSC10 shRNA cells synchronized with and released from double thymidine block to enrich for specific cell cycle phase populations. As indicated, cells were treated with Dox (shEXOSC10) and 4-OHT for 48 h before and for 48 h during synchronization and release. Etoposide (25 μM) treatment took place for 2 h before

harvest. ACTB was loading control. For pKAP1, two acquisitions of the same membrane are shown, one with longer exposure for EtOH and shEXOSC10/4-OHT samples and one with shorter exposure for etoposide samples (n=5 for shEXOSC10/4-OHT, n=2 for EtOH, etoposide).

(D) Immunoblot of SH-EP-MYCNER Dox-inducible EXOSC10 shRNA cells synchronized with double thymidine block at S-phase. Cells were treated for 48 h before and for 48 h during synchronization and release with Dox (shEXOSC10) and 4-OHT, as indicated (n=2).

(E) BLISS reads centered around called peaks showing DNA double-strand breaks in SH-EP-MYCNER Dox-inducible EXOSC10 shRNA cells. Experimental conditions are as in panel (A) (n=6).

(F) Genome browser tracks of MYCN, total RNAPII and FANCD2 ChIP-RX and BLISS at the *NUP54* locus from SH-EP-MYCNER Dox-inducible EXOSC10 shRNA cells. For FANCD2 ChIP-RX, cells were treated for 72 h with Dox (shEXOSC10) and then for 4 h with 4-OHT (200 nM) as indicated (n=1).

(G) (Left) Quantification of nuclear PLA foci between PCNA and total RNAPII in SH-EP-MYCNER Dox-inducible EXOSC10 shRNA cells. Cells were treated for 72 h with Dox (shEXOSC10) and then for 4 h with 4-OHT (200 nM), where indicated. Shown is a single-cell analysis of one representative replicate (n=3). (Right) Representative images from the quantified PLAs. Scale bar: 10 μm.

(H) DNA fork progression speed in SH-EP-MYCNER Dox-inducible EXOSC10 shRNA cells. Experimental setup is shown above the quantification, culture conditions are the same as in panel (A) (n=2).

(I) Representative DNA fiber images from quantification in panel (H).

Figure 6. ATM limits MYCN-dependent transcription elongation via BRCA1 and mRNA decapping.

(A) Immunoblot of SH-EP-MYCNER cells. Cells were treated for 5 h with 4-OHT (200 nM) and KU-60019 ATM inhibitor (100 nM) in the last 3 h of treatment, as indicated. VCL was used as loading control (n=3).

(B) Metagene plots of 4sU-seq data showing nascent RNA levels of MYCN-activated and -repressed genes in SH-EP-MYCNER cells. Cells were treated for 4 h with 4-OHT (200 nM) and KU-60019 ATM inhibitor (100 nM) as indicated, and pulsed with 4sU in the last 20 min of treatment. Shown are merged replicates (n=2).

(C) Genome browser tracks of *TAF4B* and *CDKN1A* 4sU-labelled intronic reads as examples of MYCN-activated and -repressed genes from panel (B).

(D) ChIP-qPCR showing BRCA1 binding to indicated loci in SH-EP-MYCNER cells. All primers used are proximal to the TSS. Cells were treated for 5 h with 4-OHT (200 nM) and KU-60019 (100 nM) in the last 3 h of treatment where indicated. IgG samples were derived from untreated cells. Dots indicate technical replicates (n=3).

(E) Quantification of nuclear PLA foci between DCP1A and total RNAPII. Experimental conditions as in panel (D). Shown is single-cell analysis of one representative replicate (n=3).

(F) (Top) Quantification of nuclear PLA foci between DCP1A and total RNAPII in SH-EP-MYCNER cells constitutively expressing a scrambled shRNA (shSCR) or BRCA1 shRNA (shBRCA1). Cells were treated for 4 h with 4-OHT (200 nM). Shown is a single-cell analysis of one representative replicate (n=4). (Bottom) Representative images from the quantified PLAs. Scale bar: 10 µm.

(G) Trimmed (1 %) mean read density of total and pSer2 RNAPII ChIP-RX data for MYCN-activated and -repressed genes in SH-EP-MYCNER Dox-inducible DCP1A shRNA cells. Total RNAPII plots are centered around the TSS (top), while the pSer2 RNAPII plots are centered around the TES (bottom). Cells were treated with Dox for 72 h and 4-OHT (200 nM) for 4 h, where indicated. The heatmaps above each plot indicate the p-value of the

4-OHT/EtOH difference in the presence of Dox, calculated from the density values of individual genes at each genomic location (n=2).

Figure 7. mRNA decapping prevents MYCN-dependent transcription-replication conflicts.

(A) Immunoblot of DCP1A and DNA damage response proteins in SH-EP-MYCNER cells expressing Dox-inducible shRNA targeting DCP1A. Cells were treated for 144 h with Dox (shDCP1A) and 4-OHT or for 2 h with 0.5 mM hydroxyurea (HU) or 20 μM etoposide, as indicated. VCL was used as loading control. The asterisk (*) denotes a non-specific band (n=3).

(B) Two-dimensional diagrams showing γH2A.x signal intensity relative to EdU incorporation (y-axis) and DNA content (Hoechst staining; x-axis) in EdU-pulsed SH-EP-MYCNER Dox-inducible DCP1A shRNA cells. Cells were treated for 72 h with Dox (shDCP1A) and 4-OHT, as indicated. EdU (10 μM) pulse took place in the last 30 min of culture (n=3).

(C) Quantification and cell cycle distribution of cells with high γH2A.x signal intensity from panel (B) (n=3).

(D) DNA fork progression speed in SH-EP-MYCNER Dox-inducible DCP1A shRNA cells. Experimental setup is shown above the quantification, pre-treatment for 72 h with Dox (shDCP1A) and 4-OHT, as indicated, (n=2).

(E) Representative DNA fiber images from quantification in panel (D).

(F) Quantification of nuclear PLA foci between PCNA and total RNAPII. Experimental conditions are as in panel (A). Shown are single-cell analyses of a representative experiment (n=3).

(G) Model illustrating our findings.

STAR METHODS

KEY RESOURCES TABLE

REAGENT or RESOURCE	SOURCE	IDENTIFIER
Antibodies		
Rabbit polyclonal EXOSC10	Abcam	Cat# ab50558, RRID:AB_869937, Lot# GR251505, GR3286441
Mouse polyclonal EXOSC5	Abcam	Cat# ab69699, RRID:AB_1268842, Lot# GR3234250
Rabbit polyclonal EXOSC3	Abcam	Cat# ab156683, RRID:AB_2619635, Lot# GR132701
Rabbit polyclonal DIS3	Abcam	Cat# ab176802, RRID:N/A, Lot# GR267526
Mouse monoclonal β-Actin	Sigma-Aldrich	Cat# A5441, RRID:AB_476744, Lot# 026M4780V, 079M4499V
Mouse monoclonal Vinculin	Sigma-Aldrich	Cat# V9131, RRID:AB_477629, Lot# 079M4754V
Mouse monoclonal CDK2 (D-12)	Santa Cruz Biotechnology	Cat# sc-6248, RRID:AB_627238, Lot# B0916
Mouse monoclonal RNA Polymerase II 8WG16	Covance	Cat# MMS-126R, RRID:AB_10013665, Lot# B200433
Mouse monoclonal Pol II (A-10)	Santa Cruz Biotechnology	Cat# sc-17798, RRID:AB_677355, Lot# J2219
Mouse monoclonal Pol II (F-12)	Santa Cruz Biotechnology	Cat# sc-55492, RRID:AB_630203, Lot# C0119
Mouse monoclonal pSer5 RNAPII	BioLegend	Cat# 904001, RRID:AB_2565036, Lot# B276382

Rabbit polyclonal pSer2/9 RNAPII	Abcam	Cat# ab5095, RRID:AB_304749, Lot# GR3225147, GR3231908
Mouse monoclonal RPB1	BioLegend	Cat# 920204, RRID:AB_2616695, Lot# B223109
Rabbit monoclonal FANCD2	Abcam	Cat# ab221932, RRID:N/A Lot# GR3285437-3
Rabbit polyclonal Histone H3	Abcam	Cat# ab1791, RRID:AB_302613 Lot# GR3297-878-1
Rabbit polyclonal Strep-tag II	Abcam	Cat# ab76949, RRID:AB_1524455 Lot# GR3368453-2
Mouse monoclonal MBP	New England Biolabs	Cat# E8032, RRID:AB_1559730 Lot# 0101804
Mouse monoclonal N-Myc (B8.4.B)	Santa Cruz Biotechnology	Cat# sc-53993, RRID:AB_831602, Lot# C0717, C1218, K2619
Mouse monoclonal N-Myc (NCM II 100)	Santa Cruz Biotechnology	Cat# sc-56729, RRID:AB_2266882, Lot#F0413
Rabbit monoclonal cMYC [Y69]	Abcam	Cat# ab32072, RRID:AB_731658, Lot# GR3232703
Mouse monoclonal RPA194 (C-1)	Santa Cruz Biotechnology	Cat# sc-48385, RRID:AB_675814, Lot# B2316
Rabbit monoclonal TCEA1 [EPR14821]	Abcam	Cat# ab185947, RRID:N/A, Lot# GR3247528
Rabbit polyclonal Phospho-Histone H2A.X (Ser139)	Cell Signaling Technology	Cat# 2577, RRID:AB_2118010, Lot# 13
Rabbit polyclonal KAP1 (phospho S824)	Abcam	Cat# ab70369, RRID:AB_1209417, Lot# GR3219151, GR3316128

Rabbit polyclonal KAP-1	Bethyl	Cat# A300-274A, RRID:AB_185559, Lot# A300-274A-3
Mouse monoclonal DNA-PK	Thermo Fisher Scientific	Cat# MA5-13238, RRID:AB_10988612 Lot# UE2771623A
Rabbit monoclonal phospho-DNA-PKcs (Ser2056)	Cell Signaling Technology	Cat# 68716S, RRID: N/A Lot# 1
Rabbit monoclonal ATM	Cell Signaling Technology	Cat# 2873, RRID:AB_2062659 Lot# 5
Rabbit monoclonal ATM (phospho S1981)	Abcam	Cat# ab81292, RRID:AB_1640207 Lot# GR3285525-1
Rabbit polyclonal ATR	Bethyl	Cat# A300-138A, RRID:AB_2063318 Lot# 138A-4
Rabbit polyclonal ATR (phospho T1989)	Abcam	Cat# ab227851, RRID: N/A Lot# GR3214650-15
Rabbit polyclonal Phospho RPA32 (S4/S8)	Thermo Fisher Scientific	Cat# A300-245A, RRID:AB_210547, Lot# 245A-7
Rabbit polyclonal Phospho RPA32 (S33)	Bethyl	Cat# A300-246A, RRID:AB_2180847, Lot# 246A-8
Mouse monoclonal RPA 32 kDa subunit (MA34)	Santa Cruz Biotechnology	Cat# sc-53496, RRID:AB_670974, Lot# D2711
Rabbit polyclonal Chk2, phospho (Thr68)	Cell Signaling Technology	Cat# 2661, RRID:AB_331479, Lot# 11
Mouse monoclonal Chk2 (A-11)	Santa Cruz Biotechnology	Cat# sc-17747, RRID:AB_627258, Lot# F0111
Rabbit monoclonal Phospho-Chk1 (Ser345) (133D3)	Cell Signaling Technology	Cat# 2348, RRID:AB_331212, Lot# 18
Rabbit polyclonal Chk1 (FL-476)	Santa Cruz Biotechnology	Cat# sc-7898, RRID:AB_2229488, Lot# 412

Rabbit monoclonal PCNA [EPR3821]	Abcam	Cat# ab92552, RRID:AB_10561973, Lot# GR244165
Rabbit polyclonal BRCA1	Bethyl	Cat# A300-000A, RRID:AB_67367, Lot# 000A-2
Rabbit polyclonal Dcp1a	Abcam	Cat# ab47811, RRID:AB_1566746, Lot# GR3267649
Mouse monoclonal hDcp1a (56-Y)	Santa Cruz Biotechnology	Cat# sc-100706, RRID:AB_2090408, Lot# A2119
Rabbit polyclonal Rad1 (FL-282)	Santa Cruz Biotechnology	Cat# sc-22783, RRID:AB_2098037, Lot# E2704
Rabbit polyclonal Rad9 (M-389)	Santa Cruz Biotechnology	Cat# sc-8324, RRID:AB_655048, Lot# C0503
Rabbit polyclonal HA tag	Abcam	Cat# ab9110, RRID:AB_307019, Lot# GR3257587
Goat polyclonal Anti-Rabbit IgG (H+L) Cross-Adsorbed Secondary Antibody, Alexa Fluor 488	Thermo Fisher Scientific	Cat# A-11008, RRID:AB_143165, Lot# 1735088
Goat Anti-Mouse IgG (H+L), Alexa Fluor 568 Conjugated	Molecular Probes	Cat# A-11004, RRID:AB_2534072
Goat Anti-Rabbit IgG (H+L) Highly Cross-adsorbed Antibody, Alexa Fluor 568 Conjugated	Molecular Probes	Cat# A-11036, RRID:AB_10563566
Mouse monoclonal TrueBlot ULTRA: Anti-Mouse Ig HRP	Rockland	Cat# 18-8817-31, RRID:AB_2610850, Lot# 38282
Rabbit monoclonal TrueBlot: Anti-Rabbit IgG HRP	Rockland	Cat# 18-8816-31, RRID:AB_2610847, Lot# 40107
Sheep Anti-Mouse IgG - Horseradish Peroxidase	GE Healthcare	Cat# NA931, RRID:AB_772210, Lot# 17162269

Donkey Anti-Rabbit IgG, Whole Ab ECL Antibody, HRP Conjugated	GE Healthcare	Cat# NA934, RRID:AB_772206, Lot# 17163305
Murine IgG Control Antibody, Unconjugated	Sigma-Aldrich	Cat# I5381, RRID:AB_1163670
Rabbit IgG Control Antibody, Unconjugated	Sigma-Aldrich	Cat# I5006, RRID:AB_1163659
Bacterial and Virus Strains		
pLT3GEPIR-puro-pooled shRNAs	This paper	N/A
pLT3GEPIR-puro-shEXOSC10#1	This paper	N/A
pLT3GEPIR-puro-shEXOSC10#2	This paper	N/A
pLT3GEPIR-puro-shLuciferase	This paper	N/A
pLT3GEPIR-puro-shTCEA1	This paper	N/A
pLT3GEPIR-puro-shDCP1A	This paper	N/A
pLT3GEPIR-puro-shMYCN	This paper	N/A
pRRL-puro-HA-EXOSC10mutant	This paper	N/A
pcDNA3-MYCN-wt-NT-HA	Buchel et al. (2017)	N/A
pcDNA3-empty	Buchel et al. (2017)	N/A
Chemicals, Peptides, and Recombinant Proteins		
4-hydroxytamoxifen (4-OHT)	Sigma-Aldrich	Cat# H7904
Doxycycline hyclate	Sigma-Aldrich	Cat# D9891
Benzonase nuclease purity >99% 25U/ml	Merck Millipore	Cat#70664-3
Protease inhibitor cocktail	Sigma-Aldrich	Cat# P8340
Phosphatase inhibitor cocktail #1	Sigma-Aldrich	Cat# P5726
Phosphatase inhibitor cocktail #2	Sigma-Aldrich	Cat# P0044
Ethidium bromide solution 1 %	Roth	Cat# 2218.1
Puromycin	InvivoGen	Cat# ant-pr-1

Aphidicolin	Abcam	Cat# ab142400
peqGOLD Trifast	PeqLab/WVR	Cat# 30-2010
EcoRI-HF	New England Biolabs	Cat# R3101
XhoI	New England Biolabs	Cat# R0146
AgeI-HF	New England Biolabs	Cat# R3552
SpeI-HF	New England Biolabs	Cat# R3133
AsiSI	New England Biolabs	Cat# R0630
Q5 High-Fidelity DNA polymerase	New England Biolabs	Cat# M0491
RNase A	Roth	Cat# 7156.1
Dynabead Protein A	Thermo Fisher Scientific	Cat# 10002D
Dynabead Protein G	Thermo Fisher Scientific	Cat# 10004D
Dynabeads MyOne Streptavidin T1	Thermo Fisher Scientific	Cat# 65601
Agencourt AMPure XP Beads	Beckman Coulter	Cat# A63881
Agencourt RNAClean XP Beads	Beckman Coulter	Cat# A63987
SPRIselect beads	Beckman Coulter	Cat# B23319
4-Thiouridine	Sigma-Aldrich	Cat# T4509
EZ-Link HPDP-Biotin	Thermo Fisher Scientific	Cat# 21341
Etoposide	Sigma-Aldrich	Cat# E1383
Thymidine	Sigma-Aldrich	Cat# T9250
Polyethylenimine, linear	Sigma-Aldrich	Cat# 764604
KU-60019	Sigma-Aldrich	Cat# SML1416
InstantBlue(TM) Safe Coomassie Stain	Sigma-Aldrich	Cat#ISB1L-1L
Amylose resin	New England Biolabs	Cat# E8021
Dithiothreitol (DTT)	Thermo Fisher Scientific	Cat# 20291
5-Ethynyl-2'-deoxyuridine (5-EdU)	Jena Bioscience	Cat# CLK-N001-100
AF647-Picolyl-Azide	Jena Bioscience	Cat# CLK-1300-1

Hoechst 33342	Sigma-Aldrich	Cat# B2261-25MG
Propidium iodide	Sigma-Aldrich	Cat#81845
16% Paraformaldehyde (Formaldehyde) Aqueous Solution, EM Grade	Science Services	Cat# E15710
UltraPure BSA (50 mg/mL)	Thermo Fisher Scientific	Cat# AM2616
CutSmart® Buffer	New England Biolabs	Cat# B7204S
T4 DNA Ligase Buffer	New England Biolabs	Cat# B0202S
Absolute QPCR Mix, SYBR Green, no ROX	Thermo Fischer Scientific	Cat# AB-1158/B
Quick Blunting Kit	New England Biolabs	Cat# E1201L
T4 DNA Ligase, conc.	New England Biolabs	Cat# M0202M
T4 RNA Ligase 2, truncated	New England Biolabs	Cat# M0242L
NEBNext High-Fidelity 2X PCR Master Mix	New England Biolabs	Cat# M0541L
MEGAscript T7 Transcription Kit	Thermo Fischer Scientific	Cat# AM1334
SuperScript III Reverse Transcriptase	Thermo Fischer Scientific	Cat# T18080044
RNaseOUT Recombinant Ribonuclease Inhibitor	Thermo Fischer Scientific	Cat#10777019
Duolink In Situ PLA Probe Anti-Rabbit PLUS	Sigma-Aldrich	Cat# DUO92002
Duolink In Situ PLA Probe Anti-Mouse MINUS	Sigma-Aldrich	Cat# DUO92004
Duolink In Situ Wash Buffers, Fluorescence	Sigma-Aldrich	Cat# DUO82049

ibidi Mounting Medium	Ibidi	Cat# 50001
Critical Commercial Assays		
Duolink In Situ Detection Reagents Red	Sigma-Aldrich	Cat# DUO92008
Quant-iT RiboGreen RNA Assay Kit	Thermo Fischer Scientific	Cat# R11490
Quant-iT Pico Green dsDNA assay	Thermo Fischer Scientific	Cat# P7589
QIAquick Gel Extraction Kit	QIAGEN	Cat#28704
NEBNext Ultra II Directional RNA Library Prep Kit for Illumina	New England Biolabs	Cat# E7760
NEBNext rRNA Depletion Kit	New England Biolabs	Cat# E6310
miRNeasy Mini Kit	QIAGEN	Cat# 217004
RNeasy MinElute Cleanup Kit	QIAGEN	Cat# 74204
NEBNext Ultra II DNA Library Prep Kit for Illumina	New England Biolabs	Cat# E7645S
NEBNext ChIP-Seq Library Prep Master Mix Set for Illumina	New England Biolabs	Cat#E6240
NGS Fragment High Sensitivity Analysis Kit, 1-6,000 bp, 500 samples	Agilent	DNF-474-0500
NextSeq 500/550 High Output Kit v2 (75cycles)	Illumina	Cat# FC-404-2005
Deposited Data		
Raw and analyzed data - screen	This paper	GEO: GSE164569
Raw and analyzed data - BLISS	This paper	GEO: GSE164569
Raw and analyzed data – ChIP-RX	This paper	GEO: GSE164569
Raw and analyzed data – 4sU-seq	This paper	GEO: GSE164569

Human reference genome GRCh37/hg19	Genome Reference Consortium	https://support.illumina.com/sequencing/ sequencing_software/igenome.html
Mouse reference genome mm10	Genome Reference Consortium	https://support.illumina.com/sequencing/ sequencing_software/igenome.html
Experimental Models: Cell Lines		
SH-EP-MYCNER	M. Eilers	N/A
IMR-5	A. Eggert	RRID:CVCL_1306
IMR-32	M. Schwab	RRID:CVCL_0346
NGP	A. Eggert	RRID:CVCL_2141
Kelly	A. Eggert	RRID:CVCL_2092
SH-EP	M. Schwab	RRID:CVCL_0524
SH-SY5Y	ATCC	RRID:CVCL_0019
HEK293TN	ATCC	RRID:CVCL_UL49
NIH3T3	ATCC	RRID:CVCL_0594
Oligonucleotides		
mirE_shEXOSC10 #1: TGCTGTTGACAGTGAGCGACAG GTTGAGCAAGACATGTTTTAGT GAAGCCACAGATGTAAAACATG TCTTGCTCAACCTGCTGCCTACT GCCTCGGA	Fellmann et al. (2013)	EXOSC10.794
mirE_shEXOSC10 #2: TGCTGTTGACAGTGAGCGATCC ATTGACAGTTGCACAGAATAGT GAAGCCACAGATGTATTCTGTG CAACTGTCAATGGACTGCCTAC TGCCTCGGA	Fellmann et al. (2013)	EXOSC10.2068

mirE_shTCEA1: TGCTGTTGACAGTGAGCGCAAG TAAGTTGATATTAATTAATAGTG AAGCCACAGATGTATTAATTAAT ATCAACTTACTTATGCCTACTGC CTCGGA	Pelossof, Fairchild, et al. (2017)	_6917_1409_v2
mirE_shDCP1A: TGCTGTTGACAGTGAGCGATGG GAGAAGACTGATATAGAATAGT GAAGCCACAGATGTATTCTATAT CAGTCTTCTCCCACTGCCTACT GCCTCGGA	Fellmann et al. (2013)	DCP1A.242
shSCR: GTGAGCGATCTCGCTTGGGCG	Herold et al. (2019)	N/A
shBRCA1: CTACAAGAAAGTACGAGATTTA	Fellmann et al. (2013)	BRCA1.188
Flanking pLT3GEPIR primer fwd: ACACTCTTTCCCTACACGACGC TCTTCCGATCTTAGTGAAGCCA CAGATGTA	This paper	N/A
Flanking pLT3GEPIR primer rev: GTGACTGGAGTTCAGACGTGTG CTCTTCCGATCTAAGAGATAGC AAGGTATTCAG	This paper	N/A
Screen-related oligonucleotides: Supplementary Table 2	Fellmann et al. (2013); Pelossof, Fairchild, et al. (2017)	N/A

Primers for cloning, qPCR and ChIP: Supplementary Table 3	This paper; Davidson et al. (2019); Herold et al. (2019)	N/A
BLISS-related oligonucleotides: Supplementary Table 4	This paper; Yan et al. (2017); Illumina	N/A
Recombinant DNA		
psPAX2	Addgene	Cat# 12260
pMD2.G	Addgene	Cat# 12260
pLT3GEPIR	Fellmann et al. (2013)	N/A
pcDNA3	Thermo Fisher Scientific	Cat# V79020
pIND11	Fellmann et al. (2013)	N/A
pRRL-puro	Walz et al. (2014)	N/A
pcDNA3-empty	Buchel et al. (2017)	N/A
pcDNA3-HA-MYCN-WT	Buchel et al. (2017)	N/A
pRRL-EXOSC10-mutant	This paper	N/A
Software and Algorithms		
FASTQ Generation software v1.0.0	Illumina	http://illumina.com
FastQC v0.11.3	http://www.bioinformatics.babraham.ac.uk/projects/fastqc/	https://www.bioinformatics.babraham.ac.uk/projects/fastqc/
Bowtie v2.3.2	Langmead and Salzberg (2012)	http://bowtie-bio.sourceforge.net/bowtie2/index.shtml
BEDtools v2.26.0	Quinlan and Hall (2010)	https://bedtools.readthedocs.io/en/latest/
SAMtools v1.3	Li et al. (2009)	http://www.htslib.org/

NGSplot v2.61	Shen et al. (2014)	https://github.com/shenlab-sinai/ngsplot
Harmony High Content Imaging and Analysis Software	Perkin Elmer	http://www.perkinelmer.de/product/harmony-4-8-office-hh17000001
R v4.0.0	R Core Team, (2017)	https://www.R-project.org/
UMI-tools v1.0.0	Smith, (2017)	https://umi-tools.readthedocs.io/en/latest/index.html
ImageJ v2.1.0/1.53c	Schneider et al. (2012)	http://imagej.nih.gov/ij
Prism v8.2.1	GraphPad	N/A
Integrated Genome Browser v9.1.4	Freese et al. (2016)	https://bioviz.org/
LAS-4000 mini v2.1	Fujifilm	https://www.fujifilm.com

RESOURCE AVAILABILITY

Lead contact

Further information and requests for resources and reagents should be directed to and will be fulfilled by the lead contact, Martin Eilers (martin.eilers@biozentrum.uni-wuerzburg.de).

Materials availability

No unique reagents were generated for this study.

Data and code availability

- 4sU-, ChIP-seq, BLISS and shRNA screen datasets are available at the Gene Expression Omnibus under the accession number GEO: GSE164569.
- This study did not generate any new code.
- Any additional information required to reanalyze the data reported in this paper is available from the lead contact upon request.

EXPERIMENTAL MODEL AND SUBJECT DETAILS

Cell culture

Human neuroblastoma cell lines IMR-5 (male), IMR-32 (male) and SH-EP (female) were verified by STR profiling and cultured in RPMI 1640 medium (Thermo Fisher Scientific). Human HEK293TN (female) and murine NIH3T3 (not applicable) cells were grown in DMEM (Thermo Fisher Scientific). For the human neuroblastoma cell line panel, Kelly (female) cells were grown in RPMI 1640, while SH-SY5Y (female) and NGP (male) cells were grown in DMEM. All media were supplemented with 10 % fetal bovine serum (Capricorn Scientific) and 1 % penicillin/streptomycin (P/S; Sigma-Aldrich). All cell lines were cultured at 37°C, 5 % CO_2 and routinely tested for mycoplasma contamination. Cell lines containing constructs conferring puromycin resistance were routinely re-selected by incubating in 0.5-3 µg/ml puromycin-containing medium for at least 72 h.

For double thymidine block, cells were incubated in medium containing 2 mM thymidine (Sigma-Aldrich) for 16 h, released from block by incubating in normal medium for 8 h and then re-blocked with 2 mM thymidine-containing medium for 16 h. Afterwards, cells were released by aspirating the thymidine-containing medium, washing with PBS and culturing in normal medium. Culture was terminated for downstream applications after 4 h (S-phase), 8 h (G2/M-phase) or 13-14 h (G1-phase).

For clonogenic assays, cells were grown in 6-well plates. After treatment, medium was aspirated and cells were washed with PBS, before fixing with 3.7 %v/v paraformaldehyde (PFA)/PBS for 10 min. Afterwards, cells were incubated with 0.1 %w/v crystal violet in 20 %v/v ethanol for 30 min at RT, before washing with distilled water.

Transfection, virus production and transduction

For transient plasmid transfection, 10 µg plasmid DNA were mixed with 10 µl polyethylenimine (PEI, Sigma-Aldrich) in 1 ml OptiMEM (Thermo Fisher Scientific) per transfection and incubated for 20 min at RT. Culture medium was changed to transfection medium (2 % FBS, no P/S) before addition of the plasmid-PEI mixture. The cells were incubated for 8 h before changing back to normal culture medium. In the case of ectopic protein expression (pcDNA3-HA-MYCN), cells were lysed 24 h after transfection.

For virus production, HEK293TN cells at 80 % confluence were transfected with construct-containing plasmids (pLT3GEPIR or pRRL) along with the packaging plasmids psPAX2 and pMD2.G using PEI in transfection medium. Transfection medium was replaced with normal medium 8 h after transfection and virus-containing supernatant was collected 48 h and 72 h after transfection using 0.45 µm filters. Cells were then transduced using polybrene and selected 48 h after transduction using 0.5-3 µg/ml puromycin for a minimum of 72 h.

METHOD DETAILS

General cloning

The pGEX-His_6-MBP-TEV-$MYCN^{1-154}$ plasmid was provided by the Vos lab and was used to transform XL-1 blue *E.coli* cells. After Sanger sequencing (LGC Genomics) validation, the MBP-only construct was generated by digest removal of the TEV-$MYCN^{1-154}$ sequence with SacI and BamHI at 37°C for 3 h, followed by agarose gel purification. Blunting was then carried out using the Quick Blunting Kit (New England Biolabs) following manufacturer's protocol and re-ligation with T4 DNA ligase took place overnight at 4°C. The ligation product was used to transform XL-1 blue *E.coli* cells and validation was performed by SacI/BamHI restriction.

The N-HA-EXOSC10 D313A/E315A mutant construct was ordered as a gBlock (IDT) already containing AgeI and SpeI restriction sites. After restriction digest, the construct was inserted into pRRL containing an SFFV promoter and used to transform XL-1 blue *E.coli* cells. Following Sanger sequencing verification (LGC Genomics) of the construct sequence, the plasmid DNA was used for virus production as described above.

Recombinant protein expression and purification

The pGEX-His_6-MBP-TEV-$MYCN^{1-154}$ and pGEX-His_6-MBP plasmids were used to transform Bl21(DE3)-RIL *E.coli* cells and cells were then pre-cultured overnight at 37°C. 2xYT media were inoculated and cells were grown at 37°C until OD600 of 0.4, then 1 mM IPTG was added and culture was continued for 16 h at 18°C. Cells were collected by centrifugation and resuspended in lysis buffer (500 mM NaCl, 20 mM Tris-HCl pH 7.9, 10 %v/v glycerol, 30 mM imidazole pH 8.0, 5 mM beta-mercaptoethanol) containing protease inhibitors. Cells were further lysed by sonication (5 min duration, 0.6 sec on, 0.4 sec pause, 80 % output) and pelleted. Supernatants were purified first by using the Ni-NTA purification system, the appropriate elution fractions were pooled and further purified with amylose resin. The amylose elution fractions were pooled, concentrated and subjected to size exclusion chromatography using Superdex 200 26/60 prep grade columns. Appropriate fractions were then pooled, concentrated and purified protein concentration and yield were measured. Finally, 300 ng of His_6-MBP-TEV-$MYCN^{1-154}$ and His_6-MBP constructs were loaded on Bis-Tris gels and stained with InstantBlue to verify the size of the constructs and rule out impurities.

Pooled shRNA screen

A total of 610 individual shRNAs in 10 μM concentration (IDT) targeting 105 transcription termination factors, 11 positive (5 shRNAs/target; top shRNAs from (Fellmann et al., 2013) and (Pelossof et al., 2017) and negative controls (10 for GFP and 20 for luciferase) were used. All shRNAs were combined and diluted to 330 nM end concentration. Restriction sites for XhoI and EcoRI were added with an 8 cycle PCR using appropriate primers (Table S3) and the PCR products were then purified via ethanol precipitation. After restriction digest of both the pooled shRNAs and the pLT3GEPIR vector at 37°C for 1 h, ligation took place at an shRNA:vector ratio of 15:1 overnight at 4°C. The ligation reaction was subsequently used to transform competent XL-1 blue *E.coli* cells, in a number that would guarantee a minimum of 1000-fold representation for all shRNAs. After overnight incubation at 37°C, all individual bacterial colonies were harvested, plasmid DNA was isolated and subjected to NGS to assess library distribution.

Following virus production, the virus titer was assessed and SH-EP-MYCNER cells were transduced with the appropriate volume of virus supernatant to ensure 0.1 multiplicity of infection. After puromycin selection for 96 h, 1 µg/ml doxycycline and/or 100 nM 4-OHT treatments were started and t_0 cells were pelleted, flash-frozen and kept at -80°C. Medium was changed every three days and cells were counted, split and re-seeded upon reaching confluence in numbers ensuring 1000-fold shRNA representation. Each condition was harvested after 10 population doublings, flash-frozen and kept at -80°C. The screen was carried out in two series of cultures, both consisting of biological triplicates for each condition, ultimately amounting to six replicates for each condition.

Genomic DNA (gDNA) was isolated by lysing cells in HiPure Plasmid Maxiprep kit buffer R3 (Invitrogen) with the addition of RNaseA and 10 %v/v SDS. After brief sonication, phenol-chloroform extraction was carried out with a subsequent ethanol precipitation. The shRNA hairpins were then isolated via a 24 cycle PCR using 6 µg/gDNA sample and primers targeting flanking sequences of the pLT3GEPIR vector. Afterwards, all samples were purified with ethanol precipitation and diluted to 1 ng/µl. For library preparation, indexes suitable for multiplex sequencing were added to 1 ng gDNA/sample via a 15 cycle PCR and all libraries were then purified with gel extraction.

RNA isolation and quantitative PCR

Total RNA was isolated using peqGOLD TriFast (PeqLab). Reverse transcription was carried out using 0.5-1 µg RNA template, random primers, Ribolock RNase inhibitor, dNTPs, MLV buffer and MLV reverse transcriptase. cDNA was then used in quantitative PCR (qPCR) with the appropriate primers and PowerUP SYBR Green Master Mix (Thermo Fisher Scientific). All conditions were normalized to respective β2-microglobulin for mRNA qPCRs or intronic beta-actin values for 4sU validation qPCRs.

Total and nuclear protein isolation

For total native protein isolation, a HEPES lysis buffer (20 mM HEPES pH 7.9, 150 mM NaCl, 2 mM $MgCl_2$, 0.2 %v/v NP-40, 0.5 mM EDTA, 10 %v/v glycerol) was used. Lysates were sonicated four times using 5 sec pulses at 20 % output with 10 sec pauses in-between. Afterwards, 50 U/ml benzonase (Merck) were added and all lysates were incubated for 1 h at 4°C under rotation before being cleared by two sequential centrifugations. For total denatured protein isolation, cells were lysed in RIPA buffer (50 mM HEPES pH 7.9, 140 mM NaCl, 1 mM EDTA, 0,1 %v/v SDS, 1 %v/v Triton X-100, 0,1 %w/v sodium deoxycholate). Lysates were incubated for 30 min at 4°C under rotation and then cleared by centrifugation. For nuclear native protein isolation, cells were lysed in PIPES lysis buffer (5 mM PIPES pH 8.0, 85 mM KCl, 0.5 %v/v NP-40), incubated for 10 min on ice and nuclei were then collected by centrifugation at 500 g for 10 min at 4°C. The supernatant containing cytoplasmic proteins was discarded and the nuclei were then resuspended in the HEPES lysis buffer also used for total native protein isolation and the same procedure as for total protein isolation was followed. All the above lysis buffers contained phosphatase and protease inhibitors (Sigma-Aldrich) and, where indicated, 1 µg/ml ethidium bromide (Roth). Protein concentrations were measured with the BCA assay.

Co-immunoprecipitation, in-vitro pulldown and immunoblotting

For co-immunoprecipitations, a total volume of 20 µl per IP of 1:1 A/G Dynabeads mix (Thermo Fisher Scientific) was washed with 5 mg/ml BSA/PBS and then incubated overnight at 4°C under rotation in 5 mg/ml BSA/PBS with 2.5 µg antibody against MYCN (Santa Cruz Biotechnology), EXOSC10 (Abcam), EXOSC3 (Abcam) or DIS3 (Abcam). Afterwards, the bead/antibody mix was washed with BSA/PBS, 2-4 mg of lysate were added and incubated for 6 h at 4°C under rotation. In the glycerol gradient coIPs, samples were first pre-cleared by incubating the fractions with ½ volume of only A/G beads for 1 h at 4°C rotator. After washing with HEPES lysis buffer, elution was carried out by re-suspending the beads in 2x Laemmli buffer and heating for 5 min at 95°C. The supernatants were then used in immunoblotting.

For *in-vitro* pulldowns, amylose resin was washed with water and ice-cold 5 mg/ml BSA/PBS by centrifuging in-between at 5,000 rpm for 30 sec at 4°C. All subsequent wash steps were performed as above. 8 µg of MBP or MBP-MYCN purified constructs were bound to amylose resin, while 6-7 mg of HeLa nuclear protein lysate were pre-cleared with ½ volume of resin by incubating under rotation for 2 h at 4°C. The pre-cleared nuclear protein supernatants were then added to the MBP- or MBP-MYCN-bound resin and incubation took place under rotation for 6 h at 4°C. Samples were then washed with wash buffer (50 mM NaCl, 20 mM HEPES pH 7.4, 10 %v/v glycerol, 1 mM DTT, 3 mM $MgCl_2$) and finally eluted by adding elution buffer (50 mM NaCl, 20 mM HEPES pH 7.4, 10 %v/v glycerol, 1 mM DTT, 3 mM $MgCl_2$, 100 mM maltose) and incubating for 3 min at RT. Eluates were mixed with Laemmli buffer, heated for 5 min at 95°C and used for immunoblotting.

For immunoblotting, protein lysates were loaded onto Bis-Tris gels and transferred to PVDF membranes (Merck) via wet transfer. After blocking with 5 %w/v skimmed milk in TBS-T, membranes were incubated with the appropriate antibodies overnight at 4°C. Afterwards, the membranes were probed for 1 h at RT with HRP-conjugated secondary antibodies corresponding to the organism of the primary antibodies. Images were acquired with the LAS3000 or LAS4000 Mini Imaging system (Fuji).

Glycerol gradient fractionation

Nuclear protein lysates were layered on a linear 10-30 % glycerol gradient in 1x gradient buffer (20 mM HEPES/KOH pH 7.9, 150 mM NaCl, 2 mM $MgCl_2$, 0,2 % NP-40, 0,5 mM EDTA) and separated by ultracentrifugation in a Beckman Optima L-80 XP (Beckmann Coulter) using a SW41 rotor (Beckmann Coulter) at 41,000 rpm for 16 h. Gradients were fractionated with a piston gradient fractionator (BioComp Instruments) and fractions were used either for sodium deoxycholate (DOC)/TCA precipitation or for co-immunoprecipitations. For DOC/TCA precipitation, 0.15 %w/v DOC was added to each glycerol fraction and incubated for 10 min at RT. Afterwards, 100 %w/v TCA was added and samples were incubated for 30 min on ice. Following centrifugation at 12,000 rpm for 15 min at 4°C, the pellet was washed with ice-cold

acetone. After centrifugation at 12,000 rpm for 10 min at 4°C, pellets were re-suspended in 2x Laemmli buffer for use in immunoblots.

Immunofluorescence

Cells were plated in 96-well plates (Perkin Elmer) or 18-well slides (Ibidi). For EdU pulse experiments, cells were treated for 30 min with 10 µM EdU (Jena Bioscience) alongside any potential treatment before being fixed with 4 % methanol-free PFA (Science Services) for 10 min at RT. Cells were then permeabilized with either ice-cold 100 % methanol or 0.4 %v/v Triton X-100/PBS for 20 min at -20°C or 15 min at RT, respectively, and blocked with 5 %w/v BSA/PBS for 1 h at RT. In EdU pulse experiments, newly synthesized DNA was visualized by performing a copper(I)-catalyzed azide-alkyne cycloaddition (100 mM Tris pH 8.5, 4 mM $CuSO_4$, 10 mM AFDye 647 Azide (Jena Bioscience), 10 mM L-Ascorbic Acid). Cells were then incubated with primary antibodies in blocking buffer overnight at 4°C. After washing, cells were incubated with appropriate fluorophore-conjugated secondary antibodies for 1 h at RT and subsequently 2.5 µg/ml Hoechst 33342 (Sigma-Aldrich) for 10 min at RT. 30-60 image fields per well were acquired at 40x magnification, 100% excitation and non-confocal mode. Z-stacks of 4 planes at 0.5 µm distance were made and processed with Harmony High Content Imaging and Analysis Software or R. Cells were grouped into cell cycle phase according to EdU and Hoechst staining of the control condition (more details in Bioinformatic analyses section).

Flow cytometry analysis

For propidium iodide (PI) flow cytometry, sub-confluent cells were trypsinized, pelleted and washed with ice-cold PBS, before being fixed in 80 %v/v ice-cold ethanol overnight at -20°C. Cells were then washed and re-suspended in PBS containing 36 µg/ml PI and 24 µg/ml RNase A. After a 30 min incubation at 37°C in the dark, analysis was performed.

For Annexin V/PI flow cytometry, cells were trypsinized, collected in the medium they had been cultured in, pelleted and washed with ice-cold PBS. After pelleting, cells were re-suspended in 1x Annexin V-binding buffer (10 mM HEPES pH 7.4, 140 mM NaCl and 2.5 mM $CaCl_2$) and

Annexin V/Pacific Blue Dye was added before incubating for 15 min at RT in the dark. Afterwards, Annexin V-binding buffer containing 10 µg/ml PI was added and all samples were kept on ice and in the dark until analysis.

All analyses were carried out with a BD FACSCanto II (BD Biosciences) flow cytometer using the BD FACSDIVA software.

Proximity ligation assays

For proximity ligation assays (PLA), cells were seeded in 384-well plates. Following treatment and potential EdU pulse, cells were fixed with 4 % methanol-free paraformaldehyde (Electron Microscopy Sciences) for 10 min at RT, permeabilized with ice-cold 100 % methanol for 20 min at -20°C, and blocked with 5 %w/v BSA/PBS for 1 h at RT. The ClickIT reaction, if applicable, was carried out as described above and then cells were incubated with appropriate mouse and rabbit antibody pairs in blocking buffer overnight at 4°C. After washing with TBS-T, cells were treated with plus and minus PLA probes (Duolink kit, Sigma-Aldrich) specific for rabbit and mouse antibodies, respectively, for 1 h at 37°C. After washing with PLA wash buffer A (Sigma-Aldrich), the ligation reaction took place for 30 min at 37°C. After washing with PLA wash buffer A, the *in situ* PCR amplification was carried out by incubating the cells with Alexa 568/644-conjugated oligonucleotides for 1.5-2 h at 37°C in the dark. After washing with PLA wash buffer B (Sigma-Aldrich), cells were stained with Hoechst 33452 for 10 min at RT in the dark. Finally, after washing, cells were overlayed with PBS and images were acquired within the next three days at an Operetta high-content imaging system. A minimum of 300 cells from 30-60 image fields per well were acquired at 40x magnification, 100% excitation and non-confocal mode. Z-stacks of 4 planes at 0.5 µm distance were made and processed with Harmony High Content Imaging and Analysis Software.

Spike-in chromatin immunoprecipitation and sequencing (ChIP-RX)

Following treatment, all cells were fixed by adding formaldehyde (1 %v/v end concentration) and incubating for 5 min at RT under constant rotation. Formaldehyde was quenched by

incubating the cells with 125 mM glycine for 5 min at RT under constant rotation. After washing with PBS, each condition was collected in ice-cold PBS containing protease and phosphatase inhibitors (Sigma-Aldrich) and pelleted. All lysis buffers hereafter contained protease and phosphatase inhibitors. All conditions were re-suspended PIPES lysis buffer (5 mM PIPES pH 8.0, 85 mM KCl, 0.5 %v/v NP-40) and spiked in a 1:10 ratio with murine NIH3T3 cells (all except the MYCN ChIP samples; Figure S2C). After incubating for 20 min on ice, nuclei were pelleted by centrifuging at 1,500 rpm for 5 min at 4°C. The nuclear pellets were then re-suspended in RIPA lysis buffer (50 mM HEPES pH 7.9, 140 mM NaCl, 1 mM EDTA, 0,1 %v/v SDS, 1 %v/v Triton X-100, 0,1 %w/v sodium deoxycholate) for 10 min at 4°C. Chromatin from a maximum of 30 million cells per ml lysis buffer was fragmented at a Covaris Focused Ultrasonicator M220 for 50 min per ml lysate using the appropriate program. For the FANCD2 ChIP-RX, chromatin from a maximum of 30 million cells per ml lysis buffer was fragmented at a Branson sonifier with 10 sec pulses, 30 sec pauses between pulses, at 25 % output for a duration of 30 min. Chromatin fragment size of 150-200 bp was assessed with agarose gel electrophoresis. A total volume of 100 µl/IP of 1:1 A/G Dynabeads mix (Thermo Fisher Scientific) was washed with 5 mg/ml BSA/PBS and then incubated overnight at 4°C under rotation in 5 mg/ml BSA/PBS with 15 µg antibody against MYCN (Santa Cruz Biotechnologies), FANCD2 (Abcam), total (Santa Cruz Biotechnologies), pSer2 (Abcam) or pSer5 (BioLegend) RNAPII. Chromatin samples were centrifuged at 14,000 rpm for 20 min at 4°C, and then incubated with the antibody/beads mix for 6 h at 4°C under rotation. The samples were then washed three times each with washing buffer I (20 mM Tris pH 8.1, 150 mM NaCl, 2 mM EDTA, 1 %v/v Triton X-100, 0.1 %v/v SDS), washing buffer II (20 mM Tris pH 8.1, 500 mM NaCl, 2 mM EDTA, 1 %v/v Triton X-100, 0.1 %v/v SDS), washing buffer III (10 mM Tris pH 8.1, 250 mM LiCl, 1 mM EDTA, 1 %v/v NP-40, 1 %w/v sodium deoxycholate), and finally TE buffer. Chromatin was eluted twice by incubating the beads in elution buffer (100 mM $NaHCO_3$, 1 %v/v SDS in TE buffer) for 15 min at RT under rotation. Afterwards, input and immunoprecipitation samples were de-crosslinked first by digesting with RNase A for 1 h at 37°C and overnight at 65 °C with shaking and then by digesting with proteinase K for 2 h at

45 ºC with shaking. DNA was isolated by phenol-chloroform extraction, purified with ethanol precipitation and finally quantified with the Quant-iT PicoGreen dsDNA assay (Thermo Fisher Scientific). DNA libraries were prepared using the NEBNext Ultra II DNA Library Prep Kit for Illumina (New England Biolabs).

4sU sequencing

Sub-confluent cells were treated as described in text, alongside two samples without 4sU incubation as negative controls. In the last 20 min of treatment, cells were incubated with 200 µM 4- thiouridine (4sU; Sigma-Aldrich) before being lysed using QIAzol reagent (QIAGEN). For the no-chase EXOSC10 depletion experiment, cell number was counted in each condition in order to spike with 4sU-labelled mouse T-cells, also lysed in QIAzol reagent. Total RNA extraction was carried out using the miRNeasy kit (QIAGEN) with on-column DNase digestion and RNA quantity and quality were assessed on a Nanodrop spectrophotometer and a Fragment Analyzer (Thermo Fisher Scientific), respectively. 20-40 µg RNA, with RQN values higher than 9, were then biotinylated by adding EZ-Link Biotin-HPDP (Pierce) in 0.2 mg/ml dimethylformamide and biotin labeling buffer (10 mM Tris pH 7.4, 1 mM EDTA) and incubating for 2 h at RT under rotation. Biotinylated RNA was then purified via chloroform-isoamylalcohol extraction in MaXtract high density tubes (QIAGEN). The upper aqueous phase was collected and 1/10 volume of 5 M NaCl and an equal volume of isopropanol were added. All samples were centrifuged at 20,000 g for 20 min at 4°C, the RNA pellets were washed with 75 % ethanol and centrifuged at 20,000 g for 10 min at 4°C. After drying, pellets were re-suspended in nuclease-free water. The biotinylated RNA samples were then pulled-down using Dynabeads MyOne Streptavidin T1 beads (Invitrogen) in Dynabeads washing buffer (2 M NaCl, 10 mM Tris pH 7.5, 1 mM EDTA, 0.1 %v/v Tween 20) for 15 min at RT with rotation. After stringent washing, 4sU-labelled RNA was eluted from the beads with 100 µl of freshly prepared 100 mM DTT in nuclease-free water and purified using the RNeasy MinElute kit (QIAGEN). Samples were quantified using the RiboGreen Assay (Invitrogen) and 5-20 ng RNA were used for cDNA library preparation by first depleting rRNA using the NEBNext rRNA Depletion Kit

(Human/Mouse/Rat) (New England Biolabs) and then the NEBNext Ultra II Directional RNA Library Prep Kit (New England Biolabs). cDNA libraries were amplified using appropriate multiplex index primers in 11-14 cycle PCRs, depending on the amount of RNA input.

DNA fiber assay

Cells were treated as indicated and afterwards first labelled for 20 min with 5-chloro-2-deoxyuridine (CldU, 25 μM) followed by one hour incubation with 5-iodo-2-deoxyuridine (IdU, 25 μM). Fibers were spread on glass slides and acid treated. The labelled tracks were afterwards incubated at 20 °C for one hour with rat anti-BrdU antibody (detects BrdU and CldU) and mouse anti-BrdU antibody (detects BrdU and IdU). Slides were fixed with 4 % paraformaldehyde and incubated for two hours at 20 °C with Alexa Fluor 555-conjugated goat anti-rat antibody and Alexa Fluor 488-conjugated goat anti-mouse antibody. Fiber images were acquired by fluorescence microscopy using the Axio Scope A1 running with the microscope software ZEN (Zeiss) for image acquisition and processing, the program ImageJ was used for analysis of the fibers.

BLISS

BLISS was performed essentially as described in (Mirzazadeh et al., 2018; Yan *et al.*, 2017). Cells were fixed with 3.7 %v/v paraformaldehyde, washed with PBS and either stored at 4°C or directly processed. Lysis was performed by incubation in lysis buffer 1 (10 mM Tris-HCl, 10 mM NaCl, 1 mM EDTA, 0.2 % Triton X-100, pH 8) for 1 h at 4°C, brief rinsing in PBS and incubation in lysis buffer 2 (10 mM Tris-HCl, 150 mM NaCl, 1 mM EDTA, 0.3 % SDS, pH 8) for 1 h at 37°C. Following rinsing in PBS, cells were equilibrated in CutSmart buffer (New England Biolabs) previous to blunting of double-strand breaks using Quick Blunting Kit (New England Biolabs) following manufacturer's protocol. For BLISS8, following PBS rinsing and before blunting, AsiSi (New England Biolabs) digest took place according to manufacturer's instructions. Sense and antisense adapter-oligos were annealed by heating them for 5 min at 95°C, followed by a gradual cooldown to 25 °C over a period of 45 min. Consecutive to

equilibration in CutSmart buffer (New England Biolabs) and T4 Ligase buffer (New England Biolabs) annealed adapters were dispensed on samples and ligated with T4 DNA Ligase (New England Biolabs) using manufacturer's recommendations for 16 h at 16 °C. Excess Adapters were removed by repeated rinsing in a high-salt wash buffer (10 mM Tris-HCl, 2 M NaCl, 2 mM EDTA, 0.5 % Triton X-100, pH 8). Genomic DNA was extracted in DNA extraction buffer (1 % SDS, 100 mM NaCl, 50 mM EDTA, 10 mM Tris-HCl, pH 8) supplemented with Proteinase K (1 mg/ml, Roth) for 16 h in a thermo-shaker at 55 °C. DNA was isolated by phenol-chloroform extraction and isopropanol precipitation, resuspended in TE buffer and sonicated using the Covaris Focused Ultrasonicator M220 for 1 to 2 min to achieve a fragment size of 300-500 bp. Fragment size was assessed on the Fragment Analyzer (Agilent) using the NGS Fragment High Sensitivity Analysis Kit (1-6,000 bp; Agilent). The DNA was concentrated using Agentcourt AMPure XP Beads (Beckman Coulter), transcribed into RNA and DNA digested using MEGAscript™ T7 Transcription Kit (Thermo Fischer Scientific) following manufacturer's recommendations. RNA cleanup was performed using Agencourt RNAClean XP Beads (Beckman Coulter). RNA concentration was assessed on the Fragment Analyzer (Agilent) by using Standard Sensitivity RNA Analysis Kit (Agilent). Library preparation was performed by ligating the RA3 adapter to the samples with a T4 RNA Ligase 2 (New England Biolabs) supplemented with Recombinant Ribonuclease Inhibitor (Thermo Fischer Scientific). Samples were reverse transcribed using SuperScript III Reverse Transcriptase kit (Thermo Fischer Scientific) and library indexing and amplification performed using NEBNext High-Fidelity 2X PCR Master Mix (New England Biolabs) with RP1- and desired RPI-primer. The libraries were cleaned up using Agentcourt AMPure XP Beads (Beckman Coulter), quality, quantity and fragment size assessed on the Fragment Analyzer (Agilent) using the NGS Fragment High Sensitivity Analysis Kit (1-6,000 bp; Agilent) and subsequently subjected to Illumina NextSeq 500 sequencing, according to manufacturer's instructions. Adapters and oligos were custom synthesized and Unique Molecular Identifiers (UMIs) generated by random incorporation of the four standard dNTPs using the 'Machine mixing' option.

DRIPc-seq

DRIPc-seq was adapted from (Sanz and Chedin, 2019) with additional treatments with RNase T1 and RNase III to enrich for R-loop signal.

High-throughput sequencing

Following preparation of BLISS, 4sU-, ChIP-, and pooled shRNA-sequencing libraries, the quality, quantity and the size of the PCR-amplified DNA fragments were determined with a Fragment Analyzer (Thermo Fisher Scientific). All libraries were sequenced for 75 cycles on a NextSeq500 System (Illumina) according to the manufacturer's instructions. After base calling with Illumina's FASTQ Generation software v2.19, high quality PF-clusters (according to the CASAVA filter) were selected for further analyses. The overall sequencing quality was determined with the software FastQC.

QUANTIFICATION AND STATISTICAL ANALYSIS

shRNA screen analysis

For the shRNA screen, sample-specific sequencing files (FASTQ) were mapped to a custom reference database containing the guide-stem sequences of all 611 screened shRNAs. Mapping was done using Bowtie v1.1.2 not allowing any mismatches and only reporting reads with exactly one valid alignment. For each sample, reads that successfully mapped to the reference database were counted and the counts of all samples were combined in one count matrix. Size-normalization of all samples was done based on the sample with the smallest overall count-sum. Averages were calculated for the size-normalized counts of all replicates per condition. Based on these average-values, fold changes (FCs) and log2FCs were calculated to determine enrichment or depletion of individual shRNAs between different conditions. Next, the median of the effect-strengths (log2FC) of all five shRNAs per target gene was determined. The median values were used to select hits from both biological replicate screens. Visualization of the data was done in R (version 3.4.4) utilizing the libraries "gplots" and "ggplot2".

FASTQ, BAM, bedgraph generation

For BLISS, ChIP-, and 4sU-sequencing, base calling was performed using Illumina's FASTQ Generation software v1.0.0 and sequencing quality was tested using the FastQC script.For ChIP-RX, first the sequencing quality was checked using FastQC script. To map human reads, Bowtie2 v2.2.7 61 (-N 1) was used with hg19 as reference genome. For mouse reads, mm10 was used as the reference genome. Mouse reads were used for spike-normalization based on a scaling factor calculated for each ChIP-sequencing dataset as described in (Orlando et al., 2014). The BAM files obtained after spike-normalization were sorted according to the chromosome using SAMtools v1.3.1 and converted to bedGraphs using Bedtools v2.26.0 63. MYCN-activated and repressed genes were defined by positive and negative log_2FC respectively of genes with Benjamini Hochberg q value (plus/minus OHT) less than 0.05 with an expression filter rejecting genes with less than 2 counts per million. Non- and weakly expressed genes were removed. Differentially expressed genes were called with edgeR and p-values were adjusted for multiple-testing using the Benjamini-Hochberg procedure.

For 4sU-Seq, the FASTQ generation, quality check, read mapping and differential analysis expression analysis was carried out the same way as ChIP-Sequencing, with the key difference being only the reads falling in introns were considered. Bedgraph files were generated using the genomecov function from BEDTools and the Integrated Genome Browser was used to visualize these density files. Metagene window plots of the indicated gene group were generated with NGStools.

4sU-seq volcano plot and heatmaps

In order to calculate change in gene expression between shEXOSC10 and controls cells (+/- 4-OHT) from 4sU-seq data, triplicate log_2FC values from normalized reads were calculated in R, and the fold change/p-values +/- shEXOSC10 were calculated with *limma* package in R, and plotted as volcano plot with BH-q values used as a weighted parameter for color. The resulting fold change values were transformed into a normalized matrix and used for heatmap generation in *pheatmap* package in R.

Trimmed means average density plots

For both ChIP-RX and 4sU-Seq, in order to generate averaged density plots, trimmed means (1%) were calculated over 100 bins for the genomic region, from the density of reads per gene as generated by ngs.plot.r v2.41.3 for expressed genes. These values were used for calculating standard error means as well, which were displayed for both directions around the mean value. P-value per bin was calculated via unpaired Wilcoxon test in R, and converted into negative $\log_{10}$ values, which were then transformed into color coded bins mapping to the 100 generated bins earlier using *pheatmap* package in R.

4sU-Seq GO Term enrichment analysis

For 4sU-seq GO Term enrichment analysis, all 1516 IDs of genes showing negative EtOH/shEXOSC10 $\log_2$FC were uploaded on the Enrichr online platform (Chen et al., 2013; Kuleshov et al., 2016). Results from GO Biological Process 2021 were shown along with the calculated Fisher's exact test p-values.

BLISS analysis

For BLISS, samples were demultiplexed based on their condition-specific barcodes using UMI-tools (Smith et al., 2017), allowing 1 mismatch in the barcode, and separately mapped to hg19 using Bowtie2 (Langmead and Salzberg, 2012) with default parameters. Where indicated, respective samples of biological triplicates were merged prior to mapping and collectively processed. Samples were filtered against an ENCODE Blacklist file to remove regions of high variance in mappability commonly found in satellite, centromeric and telomeric repeats (Amemiya et al., 2019) using bedtools intersect (Quinlan and Hall, 2010). To allow absolute quantification of double-strand breaks and remove PCR-introduced artifacts, duplicated reads were identified based on their UMI, grouped and deduplicated using UMI-tools (Smith *et al.*, 2017) with default parameters. For BLISS8 normalization, deduplicated reads in AsiSI specific restriction sites were counted using countBamInGRanges from the R package exomeCopy. The sample with the smallest number of AsiSI specific reads was

divided by the number of respective reads from each sample. Resulting ratio was multiplied by the total amount of deduplicated reads and samples subsequently randomly subsampled to the calculated number of reads. AsiSI specific restriction sites were generated by *in silico* digestion of the hg19 genome.

Peak calling

For FANCD2 ChIP-RX peak calling, MACS2 (https://genomebiology.biomedcentral.com/articles/10.1186/gb-2008-9-9-r137) was used with *keep-dup 5* and p-value as 1e-5 and input as control. The resulting peaks were then annotated into promoter and non-promoter regions with ChIPSeeker package in R (http://www.bioconductor.org/packages/release/bioc/html/ChIPseeker.html). Peak calling and annotation for BLISS peaks was carried out in the same way, except default p-value and all duplicate tags were used without any input file. The common peaks between FANCD2 and BLISS were generated with *intersectBed* utility in bedtools v2.26.0.

Cell cycle immunofluorescence analysis

For cell cycle immunofluorescence cells were grouped into cell cycle phases according to Hoechst and EdU intensity. The sum of Hoechst staining per nucleus was used to calculate the local minimum between the two local maxima of cell populations representing 2N and 4N DNA content and defined as cutoff to distinguish between G1- and G2-phase. Similarly, EdU staining was utilized to distinguish between EdU^{low} (G1- and G2-phase) and EdU^{high} (S-phase) cell populations. Respective cutoff values were calculated according to the control condition in each measurement. For the double thymidine block and release immunofluorescence experiment, to compare the DNA content between different stainings in form of timepoints, G1- and G2-phases were calculated as described above and all Hoechst-intensity values rescaled according to G1- and G2-maxima.

Statistical analyses

In all PLA and DNA fiber assay and box plots (Figures 5G,H, 6E,F, 7D,F, S2B,G, S3F, S4E, S6D) the boxes extend from 25th to 75th percentiles, the central line is the median and, where applicable, whiskers were plotted with the Tukey method and outliers are shown as black dots. ChIP-qPCR and qPCR bar plots (Figures 1E, 2G, 4C, 6D, S1B, S2E, S3D,E) show mean values of biological or technical triplicates, as indicated and replicates are shown as black dots. The Annexin V/PI FACS bar plots (Figures 1D, S1C) show mean values of biological replicates, which are shown as black dots, and the error bars show standard deviation (SD). In all ChIP-RX and 4sU-seq plots (Figures 3C,F, 4A, 6B,G, S2C, S3A,G, S4A, S5F) the lines show mean values and the shading indicates the standard error of the mean (SEM).

For the Annexin V/PI FACS and 4sU validation qPCR, p values were calculated with a two-tailed unpaired *t*-test assuming equal SD. *P* values for cell cycle phase distribution, PLAs, γH2A.x IF and DNA fiber assays were calculated with a two-tailed Wilcoxon rank-sum test. P values for the neuroblastoma RNA-seq data were corrected with Benjamini-Hochberg. P values <0.05 were considered statistically significant.

SUPPLEMENTARY TABLE LEGENDS

Table S1. Individual counts, median and mean log_2FC of all shRNAs used in the synthetic lethality screen, Related to Figure 1.

Table S2. mirE sequences of all shRNAs used in the screen, Related to Figure 1.

Table S3. Primer sequences used in cloning, qPCR and ChIP experiments, Related to Figures 1, 2 and 6.

Table S4. Oligonucleotide sequences used in BLISS, Related to Figure 5.

REFERENCES

Amemiya, H.M., Kundaje, A., and Boyle, A.P. (2019). The ENCODE Blacklist: Identification of Problematic Regions of the Genome. Scientific reports *9*, 9354. 10.1038/s41598-019-45839-z.

Andrulis, E.D., Werner, J., Nazarian, A., Erdjument-Bromage, H., Tempst, P., and Lis, J.T. (2002). The RNA processing exosome is linked to elongating RNA polymerase II in Drosophila. Nature *420*, 837-841. 10.1038/nature01181.

Baluapuri, A., Hofstetter, J., Dudvarski Stankovic, N., Endres, T., Bhandare, P., Vos, S.M., Adhikari, B., Schwarz, J.D., Narain, A., Vogt, M., et al. (2019). MYC Recruits SPT5 to RNA Polymerase II to Promote Processive Transcription Elongation. Mol Cell *74*, 674-687 e611. 10.1016/j.molcel.2019.02.031.

Baluapuri, A., Wolf, E., and Eilers, M. (2020). Target gene-independent functions of MYC oncoproteins. Nature reviews *21*, 255-267. 10.1038/s41580-020-0215-2.

Bayona-Feliu, A., Barroso, S., Munoz, S., and Aguilera, A. (2021). The SWI/SNF chromatin remodeling complex helps resolve R-loop-mediated transcription-replication conflicts. Nature genetics *53*, 1050-1063. 10.1038/s41588-021-00867-2.

Brannan, K., Kim, H., Erickson, B., Glover-Cutter, K., Kim, S., Fong, N., Kiemele, L., Hansen, K., Davis, R., Lykke-Andersen, J., and Bentley, D.L. (2012). mRNA decapping factors and the exonuclease Xrn2 function in widespread premature termination of RNA polymerase II transcription. Mol Cell *46*, 311-324. 10.1016/j.molcel.2012.03.006.

Buchel, G., Carstensen, A., Mak, K.Y., Roeschert, I., Leen, E., Sumara, O., Hofstetter, J., Herold, S., Kalb, J., Baluapuri, A., et al. (2017). Association with Aurora-A Controls N-MYC-Dependent Promoter Escape and Pause Release of RNA Polymerase II during the Cell Cycle. Cell reports *21*, 3483-3497. 10.1016/j.celrep.2017.11.090.

Chen, E.Y., Tan, C.M., Kou, Y., Duan, Q., Wang, Z., Meirelles, G.V., Clark, N.R., and Ma'ayan, A. (2013). Enrichr: interactive and collaborative HTML5 gene list enrichment analysis tool. BMC Bioinformatics *14*, 128. 10.1186/1471-2105-14-128.

Chiu, A.C., Suzuki, H.I., Wu, X., Mahat, D.B., Kriz, A.J., and Sharp, P.A. (2018). Transcriptional Pause Sites Delineate Stable Nucleosome-Associated Premature Polyadenylation Suppressed by U1 snRNP. Mol Cell *69*, 648-663 e647. 10.1016/j.molcel.2018.01.006.

Cortez, D., Wang, Y., Qin, J., and Elledge, S.J. (1999). Requirement of ATM-dependent phosphorylation of brca1 in the DNA damage response to double-strand breaks. Science *286*, 1162-1166. 10.1126/science.286.5442.1162.

Dang, C.V. (2012). MYC on the path to cancer. Cell *149*, 22-35. 10.1016/j.cell.2012.03.003.

Davidson, L., Francis, L., Cordiner, R.A., Eaton, J.D., Estell, C., Macias, S., Caceres, J.F., and West, S. (2019). Rapid Depletion of DIS3, EXOSC10, or XRN2 Reveals the Immediate Impact of Exoribonucleolysis on Nuclear RNA Metabolism and Transcriptional Control. Cell reports *26*, 2779-2791 e2775. 10.1016/j.celrep.2019.02.012.

de Pretis, S., Kress, T.R., Morelli, M.J., Sabo, A., Locarno, C., Verrecchia, A., Doni, M., Campaner, S., Amati, B., and Pelizzola, M. (2017). Integrative analysis of RNA polymerase II and transcriptional dynamics upon MYC activation. Genome Res *27*, 1658-1664. 10.1101/gr.226035.117.

Domingo-Prim, J., Endara-Coll, M., Bonath, F., Jimeno, S., Prados-Carvajal, R., Friedlander, M.R., Huertas, P., and Visa, N. (2019). EXOSC10 is required for RPA assembly and controlled DNA end resection at DNA double-strand breaks. Nat Commun *10*, 2135. 10.1038/s41467-019-10153-9.

Endres, T., Solvie, D., Heidelberger, J.B., Andrioletti, V., Baluapuri, A., Ade, C.P., Muhar, M., Eilers, U., Vos, S.M., Cramer, P., et al. (2021). Ubiquitylation of MYC couples transcription elongation with double-strand break repair at active promoters. Mol Cell *81*, 830-844 e813. 10.1016/j.molcel.2020.12.035.

Fellmann, C., Hoffmann, T., Sridhar, V., Hopfgartner, B., Muhar, M., Roth, M., Lai, D.Y., Barbosa, I.A., Kwon, J.S., Guan, Y., et al. (2013). An optimized microRNA backbone for effective single-copy RNAi. Cell reports *5*, 1704-1713. 10.1016/j.celrep.2013.11.020.

Fish, R.N., and Kane, C.M. (2002). Promoting elongation with transcript cleavage stimulatory factors. Biochim Biophys Acta *1577*, 287-307. 10.1016/s0167-4781(02)00459-1.

Fisher, R.P. (2020). Splice or Die: When MYC Is Driving, Transcription Needs NUAK1 to Avoid Fatal Pileups. Mol Cell *77*, 1157-1158. 10.1016/j.molcel.2020.02.025.
Garcia-Muse, T., and Aguilera, A. (2016). Transcription-replication conflicts: how they occur and how they are resolved. Nature reviews *17*, 553-563. 10.1038/nrm.2016.88.
Golding, S.E., Rosenberg, E., Valerie, N., Hussaini, I., Frigerio, M., Cockcroft, X.F., Chong, W.Y., Hummersone, M., Rigoreau, L., Menear, K.A., et al. (2009). Improved ATM kinase inhibitor KU-60019 radiosensitizes glioma cells, compromises insulin, AKT and ERK prosurvival signaling, and inhibits migration and invasion. Mol Cancer Ther *8*, 2894-2902. 10.1158/1535-7163.MCT-09-0519.
Gorthi, A., Romero, J.C., Loranc, E., Cao, L., Lawrence, L.A., Goodale, E., Iniguez, A.B., Bernard, X., Masamsetti, V.P., Roston, S., et al. (2018). EWS-FLI1 increases transcription to cause R-loops and block BRCA1 repair in Ewing sarcoma. Nature *555*, 387-391. 10.1038/nature25748.
Hamperl, S., Bocek, M.J., Saldivar, J.C., Swigut, T., and Cimprich, K.A. (2017). Transcription-Replication Conflict Orientation Modulates R-Loop Levels and Activates Distinct DNA Damage Responses. Cell *170*, 774-786 e719. 10.1016/j.cell.2017.07.043.
Hamperl, S., and Cimprich, K.A. (2016). Conflict Resolution in the Genome: How Transcription and Replication Make It Work. Cell *167*, 1455-1467. 10.1016/j.cell.2016.09.053.
Hernandez, G., Ramirez, M.J., Minguillon, J., Quiles, P., Ruiz de Garibay, G., Aza-Carmona, M., Bogliolo, M., Pujol, R., Prados-Carvajal, R., Fernandez, J., et al. (2018). Decapping protein EDC4 regulates DNA repair and phenocopies BRCA1. Nat Commun *9*, 967. 10.1038/s41467-018-03433-3.
Herold, S., Kalb, J., Buchel, G., Ade, C.P., Baluapuri, A., Xu, J., Koster, J., Solvie, D., Carstensen, A., Klotz, C., et al. (2019). Recruitment of BRCA1 limits MYCN-driven accumulation of stalled RNA polymerase. Nature *567*, 545-549. 10.1038/s41586-019-1030-9.
Izban, M.G., and Luse, D.S. (1992). The RNA polymerase II ternary complex cleaves the nascent transcript in a 3'----5' direction in the presence of elongation factor SII. Genes & development *6*, 1342-1356. 10.1101/gad.6.7.1342.
Jaenicke, L.A., von Eyss, B., Carstensen, A., Wolf, E., Xu, W., Greifenberg, A.K., Geyer, M., Eilers, M., and Popov, N. (2016). Ubiquitin-Dependent Turnover of MYC Antagonizes MYC/PAF1C Complex Accumulation to Drive Transcriptional Elongation. Mol Cell *61*, 54-67. 10.1016/j.molcel.2015.11.007.
Januszyk, K., Liu, Q., and Lima, C.D. (2011). Activities of human RRP6 and structure of the human RRP6 catalytic domain. Rna *17*, 1566-1577. 10.1261/rna.2763111.
Kalkat, M., Resetca, D., Lourenco, C., Chan, P.K., Wei, Y., Shiah, Y.J., Vitkin, N., Tong, Y., Sunnerhagen, M., Done, S.J., et al. (2018). MYC Protein Interactome Profiling Reveals Functionally Distinct Regions that Cooperate to Drive Tumorigenesis. Mol Cell *72*, 836-848 e837. 10.1016/j.molcel.2018.09.031.
Kilchert, C., Wittmann, S., and Vasiljeva, L. (2016). The regulation and functions of the nuclear RNA exosome complex. Nature reviews *17*, 227-239. 10.1038/nrm.2015.15.
Kress, T.R., Sabo, A., and Amati, B. (2015). MYC: connecting selective transcriptional control to global RNA production. Nat Rev Cancer *15*, 593-607. 10.1038/nrc3984.
Kuleshov, M.V., Jones, M.R., Rouillard, A.D., Fernandez, N.F., Duan, Q., Wang, Z., Koplev, S., Jenkins, S.L., Jagodnik, K.M., Lachmann, A., et al. (2016). Enrichr: a comprehensive gene set enrichment analysis web server 2016 update. Nucleic Acids Res *44*, W90-97. 10.1093/nar/gkw377.
Langmead, B., and Salzberg, S.L. (2012). Fast gapped-read alignment with Bowtie 2. Nature methods *9*, 357-359. 10.1038/nmeth.1923.
Lemay, J.F., Larochelle, M., Marguerat, S., Atkinson, S., Bahler, J., and Bachand, F. (2014). The RNA exosome promotes transcription termination of backtracked RNA polymerase II. Nat Struct Mol Biol *21*, 919-926. 10.1038/nsmb.2893.
Li, H., Handsaker, B., Wysoker, A., Fennell, T., Ruan, J., Homer, N., Marth, G., Abecasis, G., Durbin, R., and Genome Project Data Processing, S. (2009). The Sequence Alignment/Map format and SAMtools. Bioinformatics *25*, 2078-2079. 10.1093/bioinformatics/btp352.

Lingaraju, M., Schuller, J.M., Falk, S., Gerlach, P., Bonneau, F., Basquin, J., Benda, C., and Conti, E. (2019). To Process or to Decay: A Mechanistic View of the Nuclear RNA Exosome. Cold Spring Harb Symp Quant Biol *84*, 155-163. 10.1101/sqb.2019.84.040295.
Lourenco, C., Resetca, D., Redel, C., Lin, P., MacDonald, A.S., Ciaccio, R., Kenney, T.M.G., Wei, Y., Andrews, D.W., Sunnerhagen, M., et al. (2021). MYC protein interactors in gene transcription and cancer. Nat Rev Cancer. 10.1038/s41568-021-00367-9.
Lubas, M., Christensen, M.S., Kristiansen, M.S., Domanski, M., Falkenby, L.G., Lykke-Andersen, S., Andersen, J.S., Dziembowski, A., and Jensen, T.H. (2011). Interaction profiling identifies the human nuclear exosome targeting complex. Mol Cell *43*, 624-637. 10.1016/j.molcel.2011.06.028.
Ma, J., Bai, L., and Wang, M.D. (2013). Transcription under torsion. Science *340*, 1580-1583. 10.1126/science.1235441.
Ma, J., Tan, C., Gao, X., Fulbright, R.M., Jr., Roberts, J.W., and Wang, M.D. (2019). Transcription factor regulation of RNA polymerase's torque generation capacity. Proceedings of the National Academy of Sciences of the United States of America *116*, 2583-2588. 10.1073/pnas.1807031116.
Macheret, M., and Halazonetis, T.D. (2018). Intragenic origins due to short G1 phases underlie oncogene-induced DNA replication stress. Nature *555*, 112-116. 10.1038/nature25507.
Macias, S., Cordiner, R.A., Gautier, P., Plass, M., and Caceres, J.F. (2015). DGCR8 Acts as an Adaptor for the Exosome Complex to Degrade Double-Stranded Structured RNAs. Mol Cell *60*, 873-885. 10.1016/j.molcel.2015.11.011.
Marin-Vicente, C., Domingo-Prim, J., Eberle, A.B., and Visa, N. (2015). RRP6/EXOSC10 is required for the repair of DNA double-strand breaks by homologous recombination. Journal of cell science *128*, 1097-1107. 10.1242/jcs.158733.
Mirzazadeh, R., Kallas, T., Bienko, M., and Crosetto, N. (2018). Genome-Wide Profiling of DNA Double-Strand Breaks by the BLESS and BLISS Methods. Methods Mol Biol *1672*, 167-194. 10.1007/978-1-4939-7306-4_14.
Noe Gonzalez, M., Blears, D., and Svejstrup, J.Q. (2020). Causes and consequences of RNA polymerase II stalling during transcript elongation. Nature reviews. 10.1038/s41580-020-00308-8.
Orlando, D.A., Chen, M.W., Brown, V.E., Solanki, S., Choi, Y.J., Olson, E.R., Fritz, C.C., Bradner, J.E., and Guenther, M.G. (2014). Quantitative ChIP-Seq normalization reveals global modulation of the epigenome. Cell reports *9*, 1163-1170. 10.1016/j.celrep.2014.10.018.
Palangat, M., Renner, D.B., Price, D.H., and Landick, R. (2005). A negative elongation factor for human RNA polymerase II inhibits the anti-arrest transcript-cleavage factor TFIIS. Proceedings of the National Academy of Sciences of the United States of America *102*, 15036-15041. 10.1073/pnas.0409405102.
Pelossof, R., Fairchild, L., Huang, C.H., Widmer, C., Sreedharan, V.T., Sinha, N., Lai, D.Y., Guan, Y., Premsrirut, P.K., Tschaharganeh, D.F., et al. (2017). Prediction of potent shRNAs with a sequential classification algorithm. Nat Biotechnol *35*, 350-353. 10.1038/nbt.3807.
Petryk, N., Kahli, M., d'Aubenton-Carafa, Y., Jaszczyszyn, Y., Shen, Y., Silvain, M., Thermes, C., Chen, C.L., and Hyrien, O. (2016). Replication landscape of the human genome. Nat Commun *7*, 10208. 10.1038/ncomms10208.
Phatnani, H.P., and Greenleaf, A.L. (2006). Phosphorylation and functions of the RNA polymerase II CTD. Genes & development *20*, 2922-2936. 10.1101/gad.1477006.
Poli, J., Gerhold, C.B., Tosi, A., Hustedt, N., Seeber, A., Sack, R., Herzog, F., Pasero, P., Shimada, K., Hopfner, K.P., and Gasser, S.M. (2016). Mec1, INO80, and the PAF1 complex cooperate to limit transcription replication conflicts through RNAPII removal during replication stress. Genes & development *30*, 337-354. 10.1101/gad.273813.115.
Proudfoot, N.J. (2016). Transcriptional termination in mammals: Stopping the RNA polymerase II juggernaut. Science *352*, aad9926. 10.1126/science.aad9926.
Quinlan, A.R., and Hall, I.M. (2010). BEDTools: a flexible suite of utilities for comparing genomic features. Bioinformatics *26*, 841-842. 10.1093/bioinformatics/btq033.
Rahl, P.B., Lin, C.Y., Seila, A.C., Flynn, R.A., McCuine, S., Burge, C.B., Sharp, P.A., and Young, R.A. (2010). c-Myc regulates transcriptional pause release. Cell *141*, 432-445. 10.1016/j.cell.2010.03.030.

Reines, D., Chamberlin, M.J., and Kane, C.M. (1989). Transcription elongation factor SII (TFIIS) enables RNA polymerase II to elongate through a block to transcription in a human gene in vitro. The Journal of biological chemistry *264*, 10799-10809.
Richard, P., Feng, S., and Manley, J.L. (2013). A SUMO-dependent interaction between Senataxin and the exosome, disrupted in the neurodegenerative disease AOA2, targets the exosome to sites of transcription-induced DNA damage. Genes & development *27*, 2227-2232. 10.1101/gad.224923.113.
Rickman, D.S., Schulte, J.H., and Eilers, M. (2018). The Expanding World of N-MYC-Driven Tumors. Cancer Discov *8*, 150-163. 10.1158/2159-8290.CD-17-0273.
Roeschert, I., Poon, E., Henssen, A.G., Dorado Garcia, H., Gatti, M., Giansanti, C., Jamin, Y., Ade, C.P., Gallant, P., Schülein-Völk, C., et al. (2021). Combined inhibition of Aurora-A and ATR kinases results in regression of MYCN-amplified neuroblastoma. Nature Cancer. 10.1038/s43018-020-00171-8.
Sanz, L.A., and Chedin, F. (2019). High-resolution, strand-specific R-loop mapping via S9.6-based DNA-RNA immunoprecipitation and high-throughput sequencing. Nature protocols *14*, 1734-1755. 10.1038/s41596-019-0159-1.
Shen, L., Shao, N., Liu, X., and Nestler, E. (2014). ngs.plot: Quick mining and visualization of next-generation sequencing data by integrating genomic databases. BMC Genomics *15*, 284. 10.1186/1471-2164-15-284.
Sheridan, R.M., Fong, N., D'Alessandro, A., and Bentley, D.L. (2019). Widespread Backtracking by RNA Pol II Is a Major Effector of Gene Activation, 5' Pause Release, Termination, and Transcription Elongation Rate. Mol Cell *73*, 107-118 e104. 10.1016/j.molcel.2018.10.031.
Silla, T., Schmid, M., Dou, Y., Garland, W., Milek, M., Imami, K., Johnsen, D., Polak, P., Andersen, J.S., Selbach, M., et al. (2020). The human ZC3H3 and RBM26/27 proteins are critical for PAXT-mediated nuclear RNA decay. Nucleic Acids Res *48*, 2518-2530. 10.1093/nar/gkz1238.
Smith, T., Heger, A., and Sudbery, I. (2017). UMI-tools: modeling sequencing errors in Unique Molecular Identifiers to improve quantification accuracy. Genome Res *27*, 491-499. 10.1101/gr.209601.116.
Venkitaraman, A.R. (2014). Cancer suppression by the chromosome custodians, BRCA1 and BRCA2. Science *343*, 1470-1475. 10.1126/science.1252230.
Walz, S., Lorenzin, F., Morton, J., Wiese, K.E., von Eyss, B., Herold, S., Rycak, L., Dumay-Odelot, H., Karim, S., Bartkuhn, M., et al. (2014). Activation and repression by oncogenic MYC shape tumour-specific gene expression profiles. Nature *511*, 483-487. 10.1038/nature13473.
Yan, W.X., Mirzazadeh, R., Garnerone, S., Scott, D., Schneider, M.W., Kallas, T., Custodio, J., Wernersson, E., Li, Y., Gao, L., et al. (2017). BLISS is a versatile and quantitative method for genome-wide profiling of DNA double-strand breaks. Nat Commun *8*, 15058. 10.1038/ncomms15058.
Zatreanu, D., Han, Z., Mitter, R., Tumini, E., Williams, H., Gregersen, L., Dirac-Svejstrup, A.B., Roma, S., Stewart, A., Aguilera, A., and Svejstrup, J.Q. (2019). Elongation Factor TFIIS Prevents Transcription Stress and R-Loop Accumulation to Maintain Genome Stability. Mol Cell *76*, 57-69 e59. 10.1016/j.molcel.2019.07.037.
Zhang, X., Chiang, H.C., Wang, Y., Zhang, C., Smith, S., Zhao, X., Nair, S.J., Michalek, J., Jatoi, I., Lautner, M., et al. (2017). Attenuation of RNA polymerase II pausing mitigates BRCA1-associated R-loop accumulation and tumorigenesis. Nat Commun *8*, 15908. 10.1038/ncomms15908.
Zinder, J.C., and Lima, C.D. (2017). Targeting RNA for processing or destruction by the eukaryotic RNA exosome and its cofactors. Genes & development *31*, 88-100. 10.1101/gad.294769.116.

Figure 1

Figure 1 (Papadopoulos et al.)

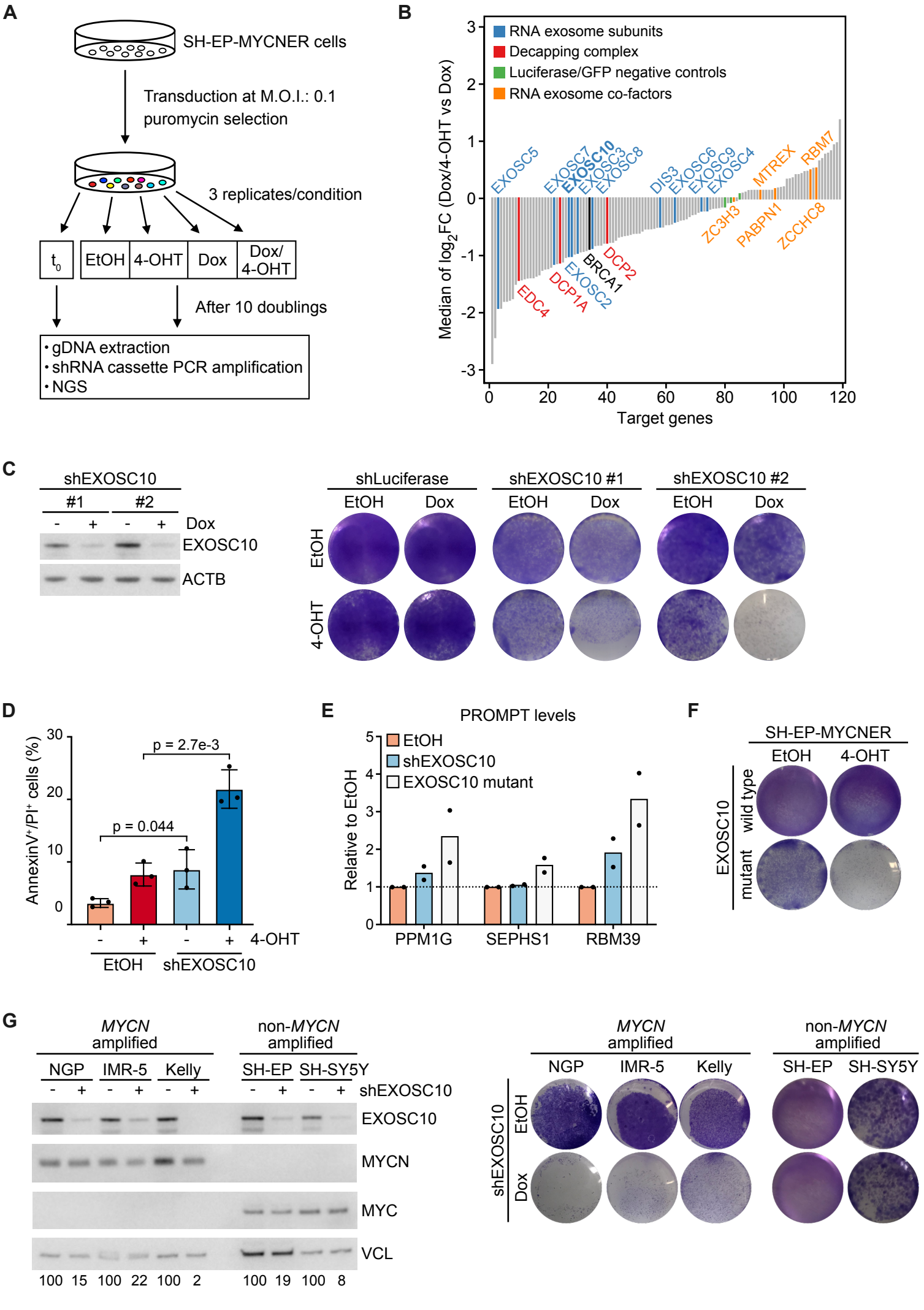

Figure 2

Figure 2 (Papadopoulos et al.)

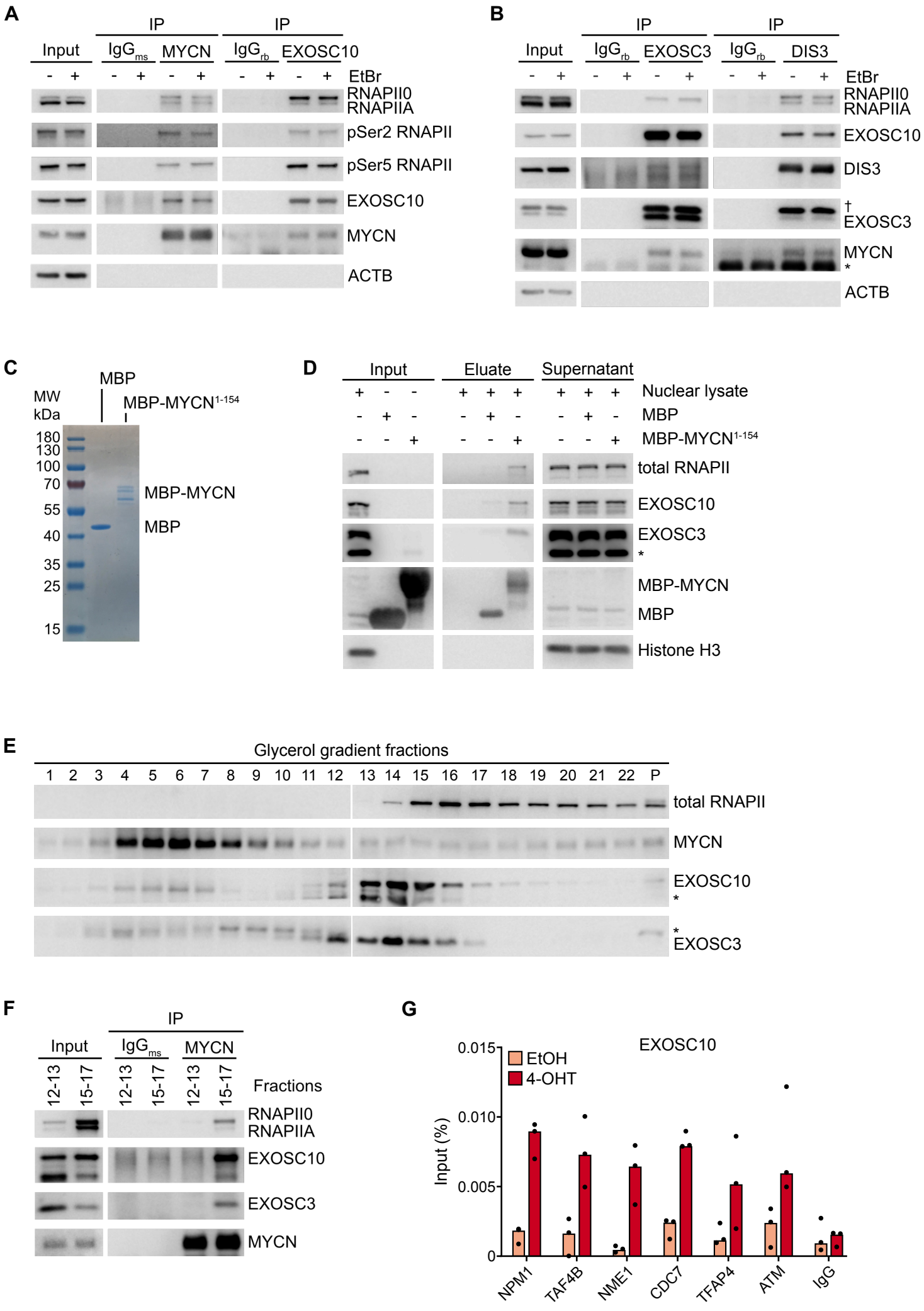

Figure 3

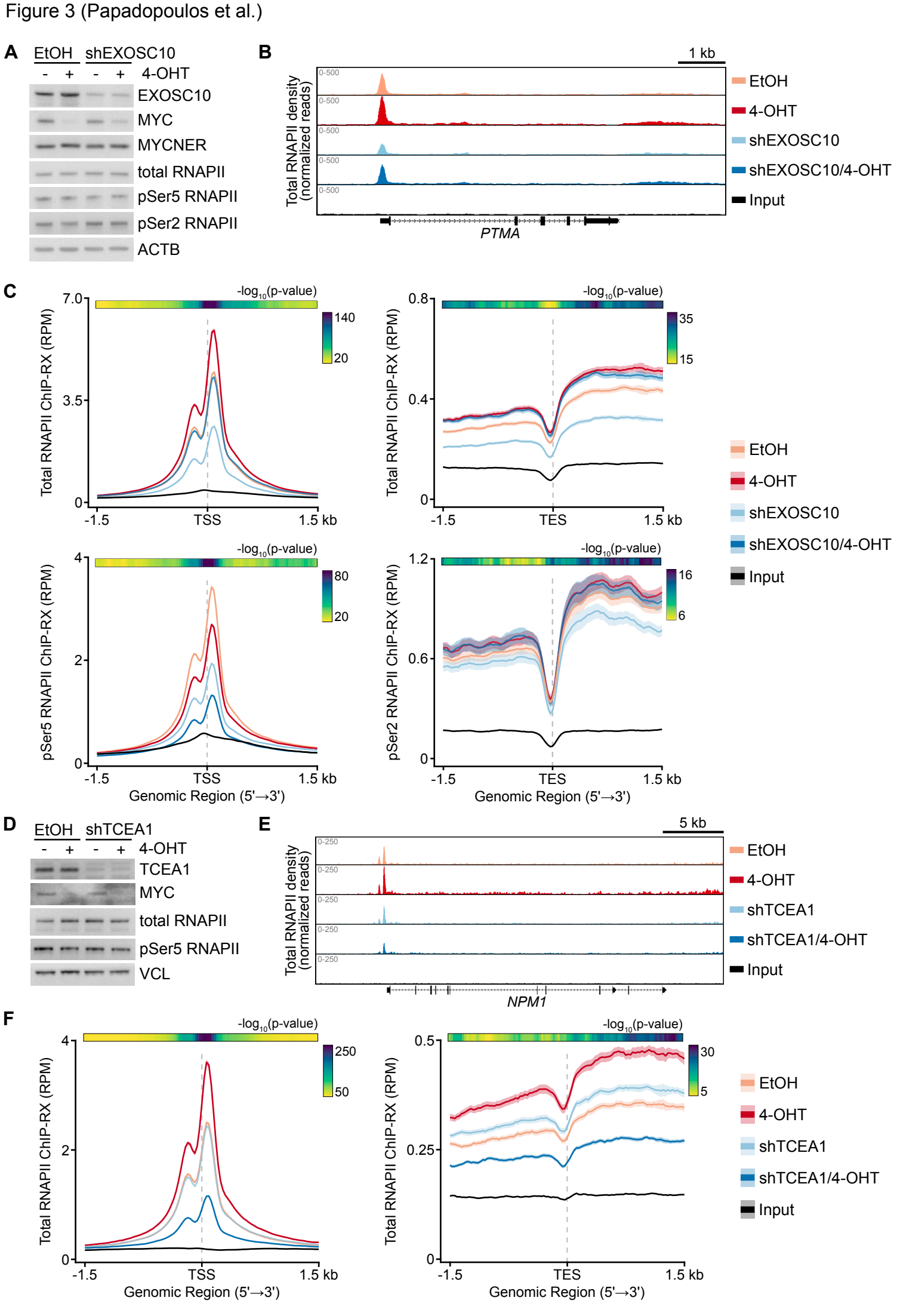
Figure 3 (Papadopoulos et al.)
A
EtOH
shEXOSC10
- + - +
4-OHT
EXOSC10
MYC
MYCNER
total RNAPII
pSer5 RNAPII
pSer2 RNAPII
ACTB
B
1 kb
Total RNAPII density (normalized reads)
0-500
EtOH
4-OHT
shEXOSC10
shEXOSC10/4-OHT
Input
PTMA
C
-log10(p-value)
Total RNAPII ChIP-RX (RPM)
pSer5 RNAPII ChIP-RX (RPM)
pSer2 RNAPII ChIP-RX (RPM)
-1.5
TSS
TES
1.5 kb
Genomic Region (5'→3')
EtOH
4-OHT
shEXOSC10
shEXOSC10/4-OHT
Input
D
EtOH
shTCEA1
- + - +
4-OHT
TCEA1
MYC
total RNAPII
pSer5 RNAPII
VCL
E
5 kb
Total RNAPII density (normalized reads)
0-250
EtOH
4-OHT
shTCEA1
shTCEA1/4-OHT
Input
NPM1
F
-log10(p-value)
Total RNAPII ChIP-RX (RPM)
-1.5
TSS
TES
1.5 kb
Genomic Region (5'→3')
EtOH
4-OHT
shTCEA1
shTCEA1/4-OHT
Input

Figure 4

Figure 4 (Papadopoulos et al.)

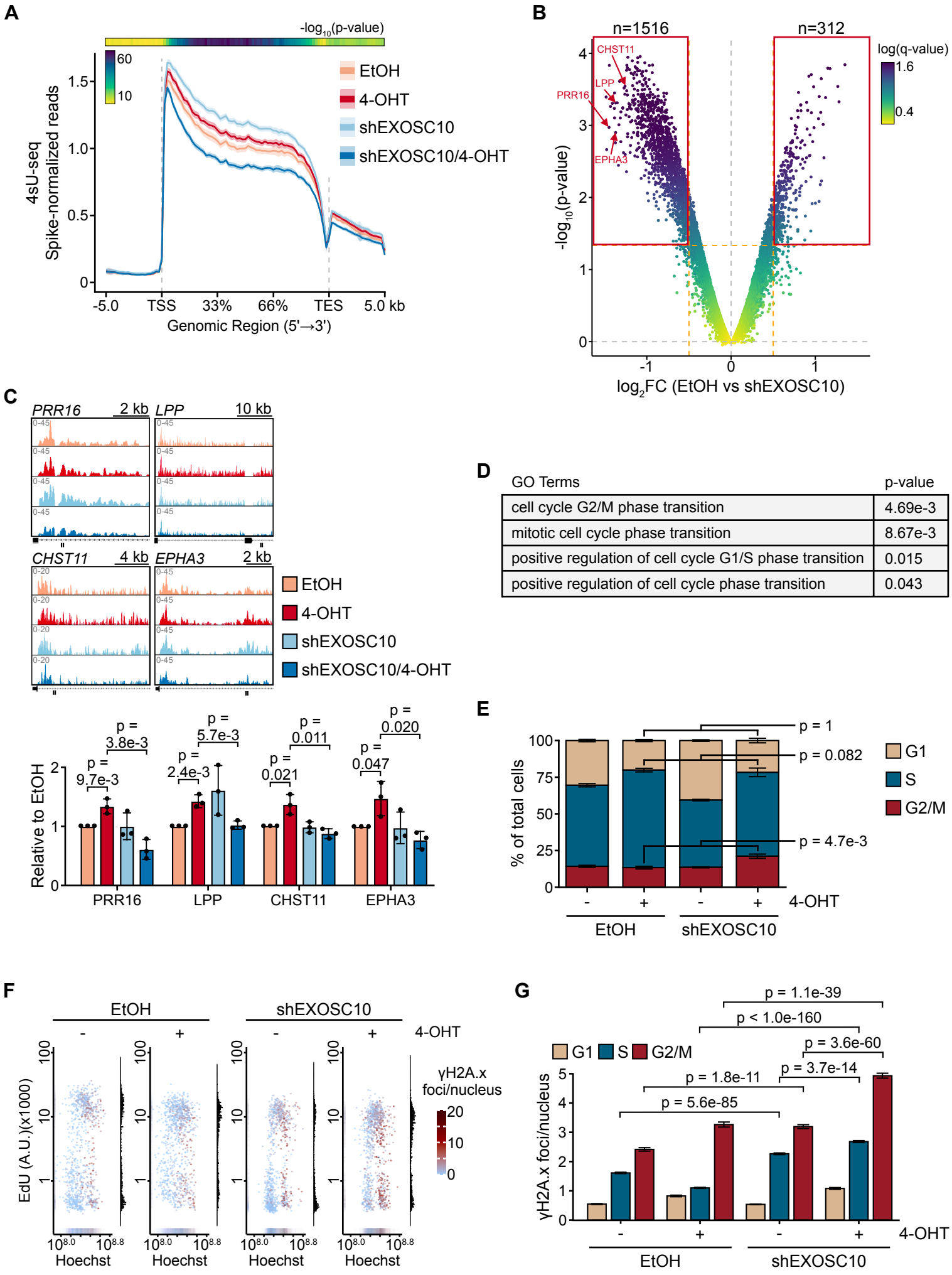

Figure 5

Figure 5 (Papadopoulos et al.)

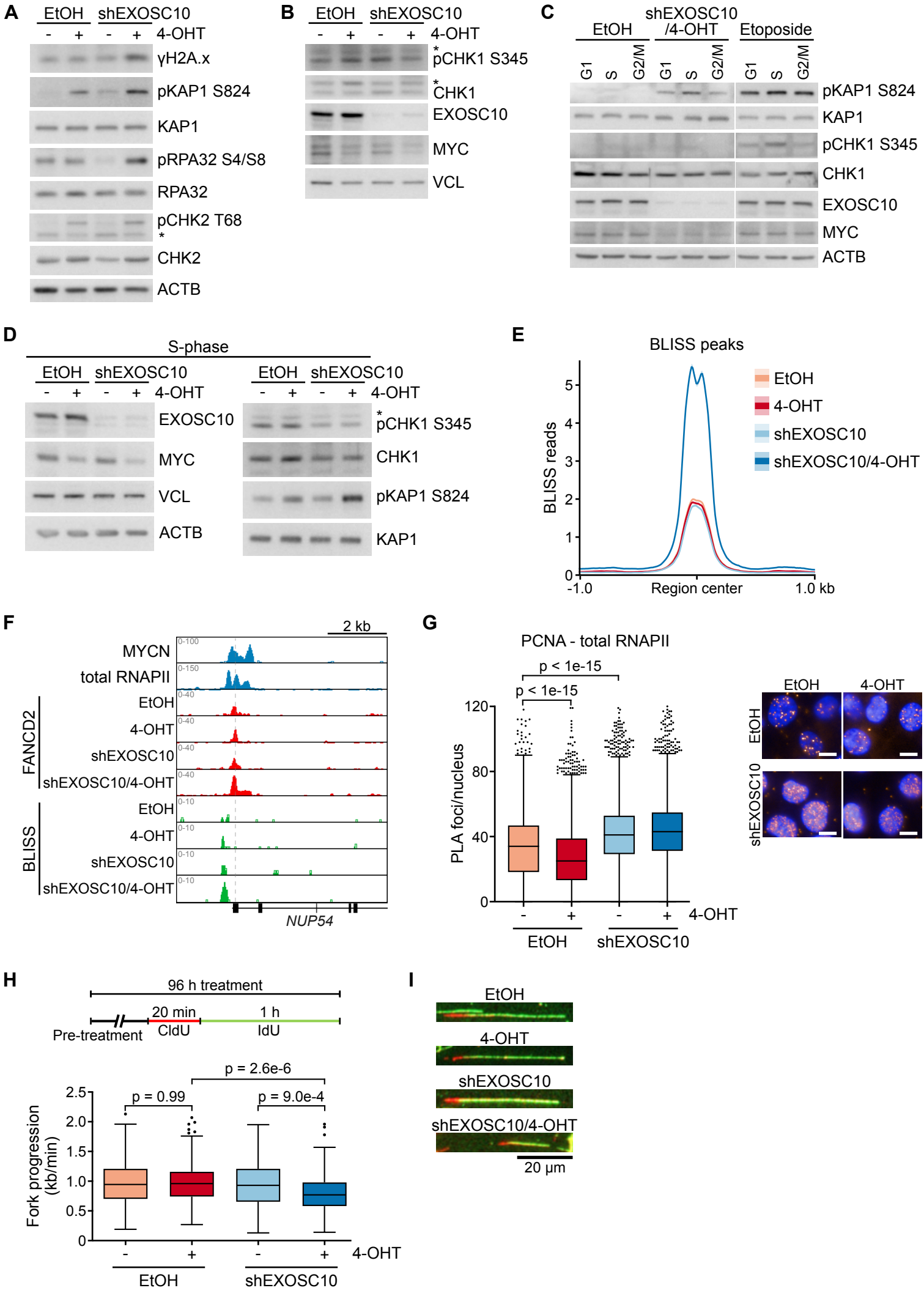

Figure 6

Figure 6 (Papadopoulos et al.)

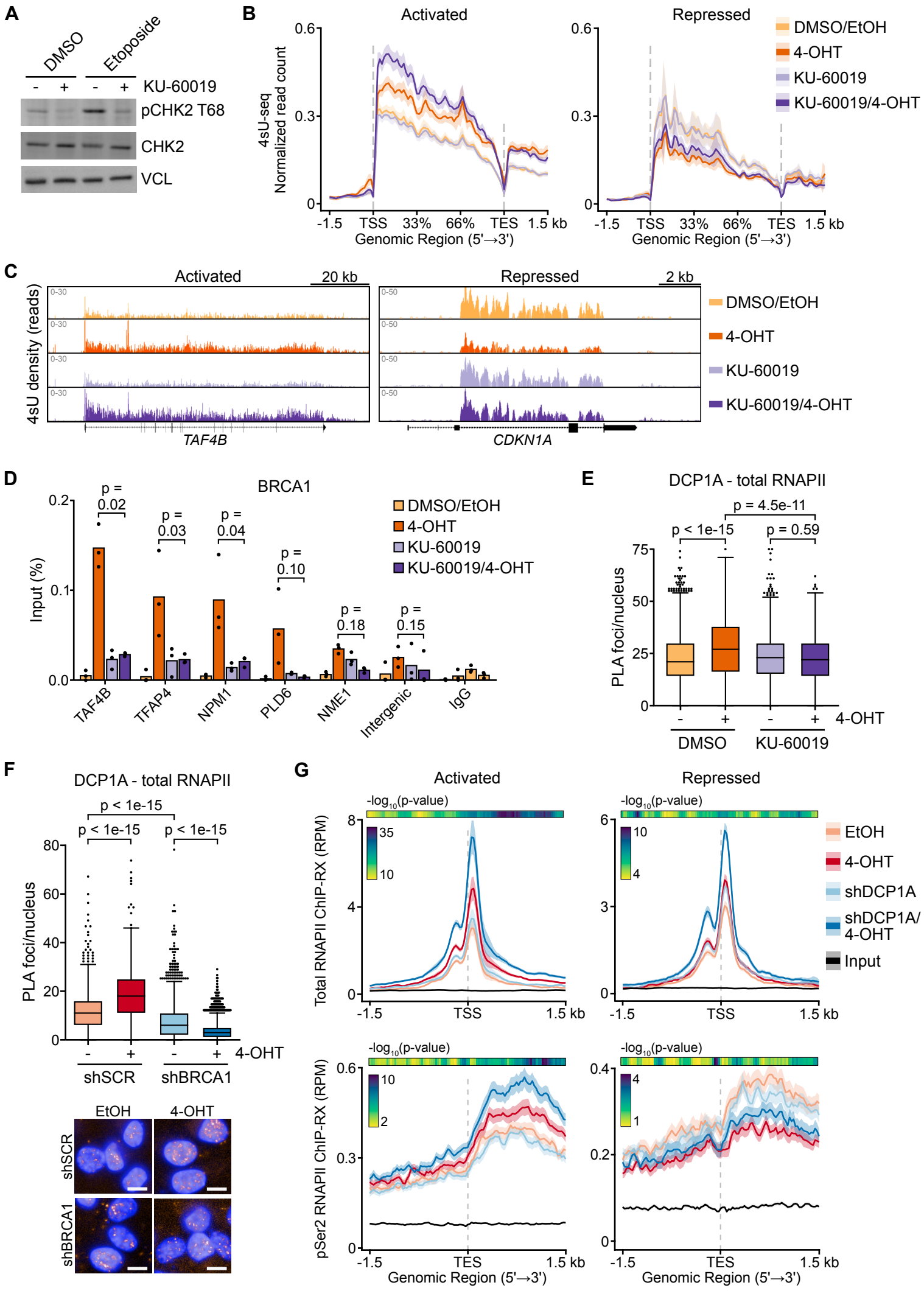

Figure 7

Figure 7 (Papadopoulos et al.)

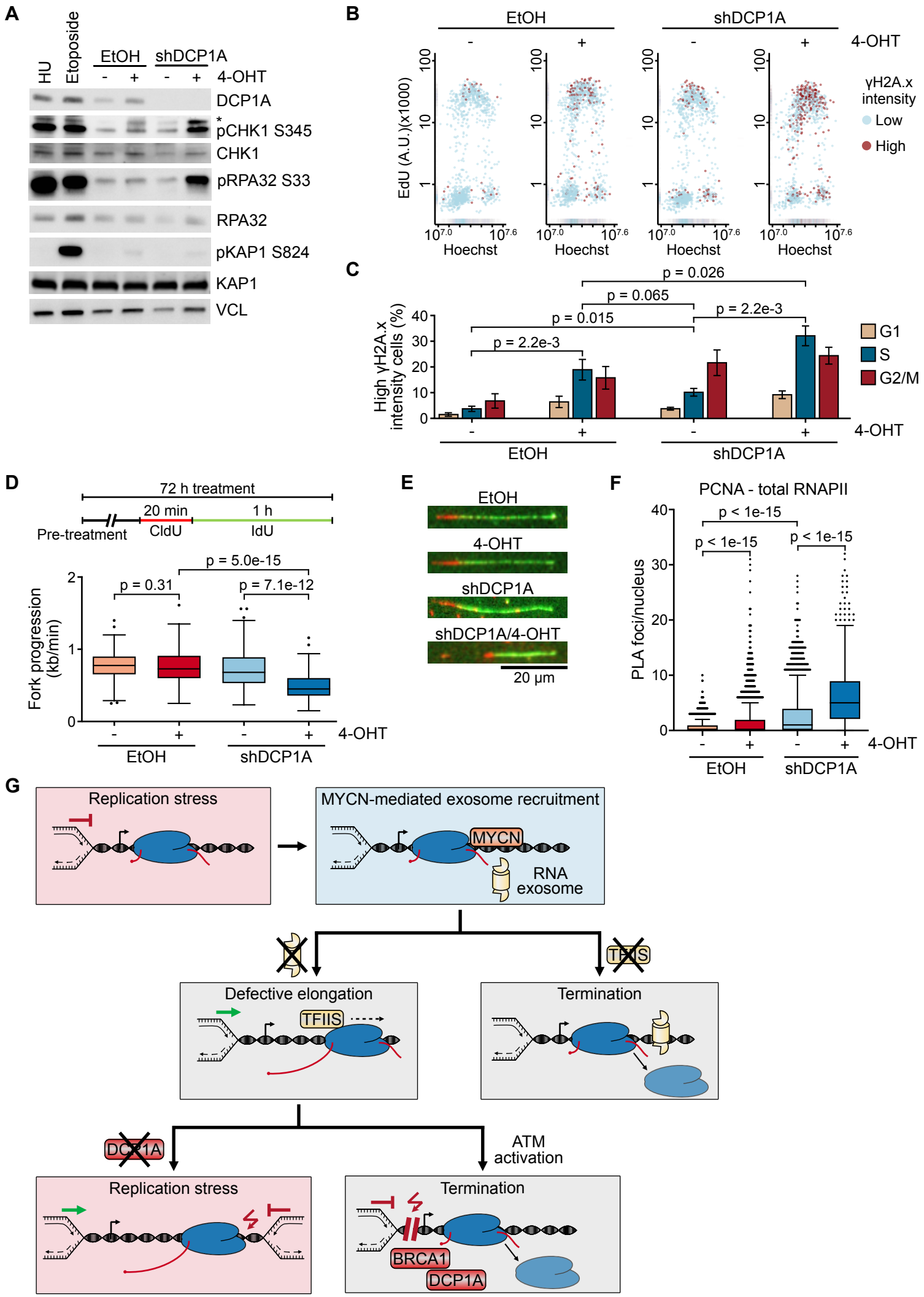

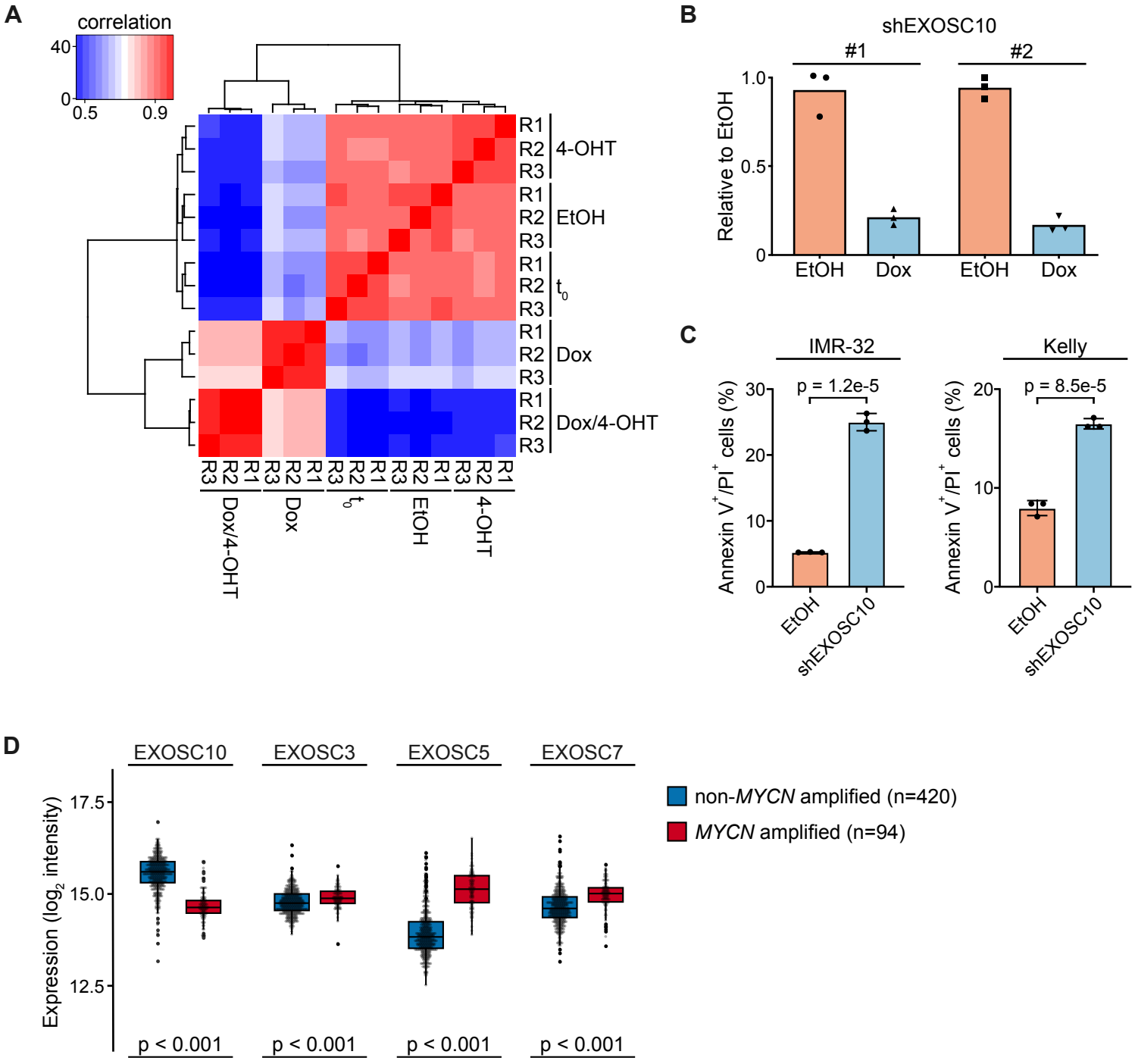

Figure S1. Nuclear RNA exosome function is critical for MYCN-driven proliferation. Related to Figure 1.

(A) Heatmap of Spearman correlation coefficients showing the relationship of normalized shRNA counts among all conditions in the shRNA screen.

(B) qPCR of EXOSC10 mRNA in SH-EP-MYCNER cells expressing Dox-inducible shRNAs targeting EXOSC10 after 72 h of Dox treatment. Dots indicate biological replicates (n=3).

(C) Annexin V/propidium iodide FACS analysis of IMR-32 and Kelly cells expressing Dox-inducible EXOSC10 shRNA in control (EtOH) and after 96 h of Dox (shEXOSC10) incubation. Dots indicate biological replicates (n=3).

(D) RNA-seq data of primary neuroblastoma patient samples showing log_2 expression levels of indicated genes stratified for *MYCN* amplification status.

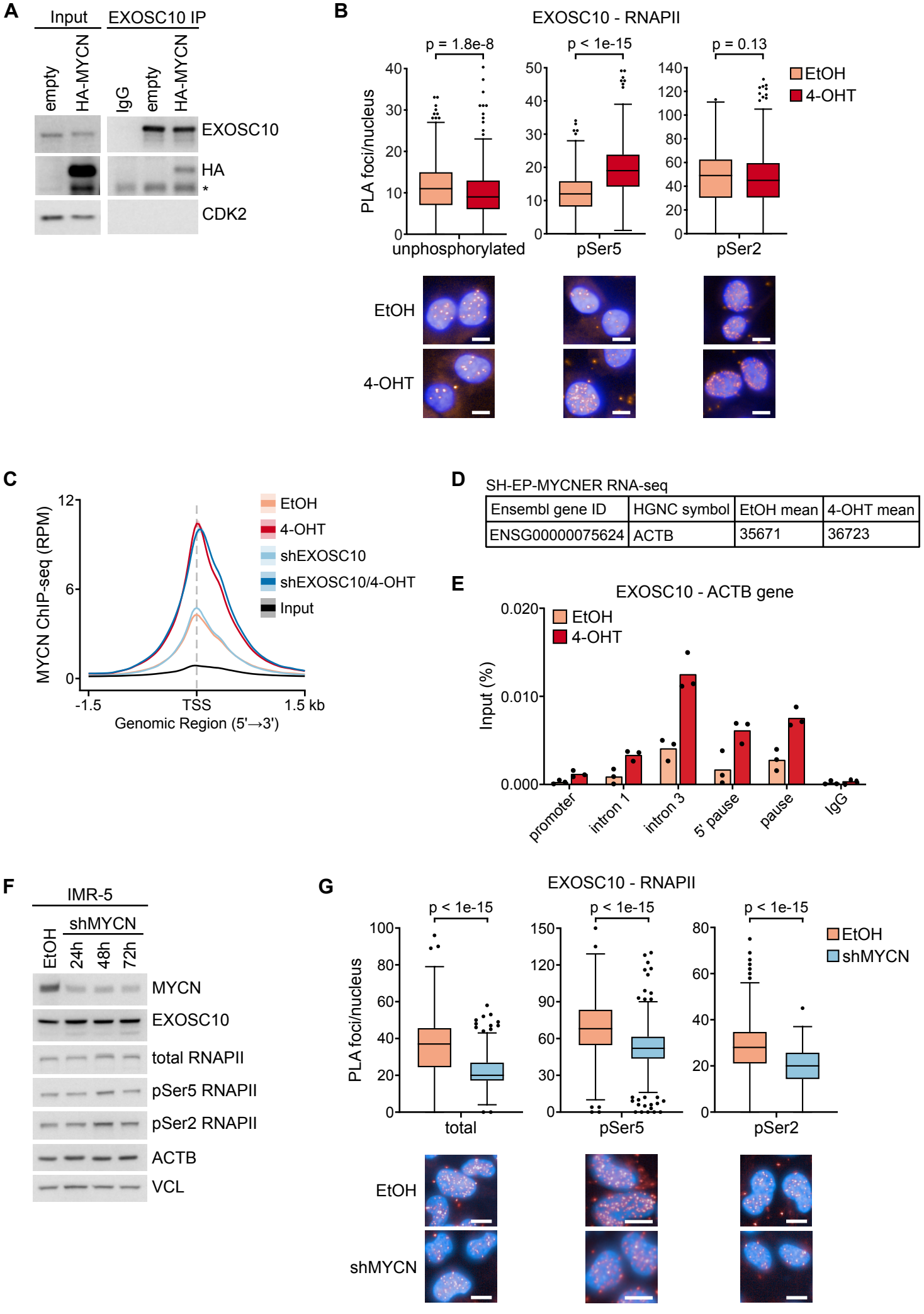
A
Input
EXOSC10 IP
empty
HA-MYCN
IgG
empty
HA-MYCN
EXOSC10
HA
*
CDK2
B
EXOSC10 - RNAPII
p = 1.8e-8
p < 1e-15
p = 0.13
PLA foci/nucleus
unphosphorylated
pSer5
pSer2
EtOH
4-OHT
C
MYCN ChIP-seq (RPM)
EtOH
4-OHT
shEXOSC10
shEXOSC10/4-OHT
Input
-1.5
TSS
1.5 kb
Genomic Region (5'→3')
D
SH-EP-MYCNER RNA-seq
Ensembl gene ID
HGNC symbol
EtOH mean
4-OHT mean
ENSG00000075624
ACTB
35671
36723
E
EXOSC10 - ACTB gene
Input (%)
promoter
intron 1
intron 3
5' pause
pause
IgG
F
IMR-5
shMYCN
EtOH
24h
48h
72h
MYCN
EXOSC10
total RNAPII
pSer5 RNAPII
pSer2 RNAPII
ACTB
VCL
G
EXOSC10 - RNAPII
p < 1e-15
p < 1e-15
p < 1e-15
PLA foci/nucleus
total
pSer5
pSer2
EtOH
shMYCN

Figure S2. MYCN recruits the RNA exosome to its target promoters. Related to Figure 2.

(A) Immunoblot of EXOSC10 IP from SH-EP cells transfected with an HA-tagged human MYCN construct or control vector. CDK2 was loading control. Asterisk denotes the antibody heavy chain (n=3).

(B) (Top) Quantification of nuclear PLA foci between EXOSC10 and unphosphorylated, pSer5 or pSer2 RNAPII in SH-EP-MYCNER cells after 4 h 4-OHT (200 nM) treatment. Shown is the single-cell analysis from representative experiments (n=3). (Bottom) Representative images from the quantified PLAs. Scale bar: 10 µm.

(C) Mean read density plot centered around TSS showing MYCN ChIP-seq data for expressed genes (>8 kb) (n=1).

(D) RNA-seq data showing mean ACTB mRNA levels in SH-EP-MYCNER cells treated for 3 h with 4-OHT (200 nM) (n=3). Data are taken from (Herold et al., 2019).

(E) ChIP-qPCR showing EXOSC10 binding to indicated loci in the *ACTB* gene in SH-EP-MYCNER cells. Cells were treated for 4 h with 4-OHT (200 nM), where indicated. Dots indicate technical replicates (n=2).

(F) Immunoblot of IMR-5 cells expressing two different Dox-inducible shRNAs against MYCN. Cells were treated with Dox (shMYCN) for the indicated times (n=2).

(G) (Top) Quantification of nuclear PLA foci between EXOSC10 and total, pSer5 or pSer2 RNAPII in IMR-5 double shMYCN cells. Cells were treated for 48 h with Dox (shMYCN), as indicated. Shown is the single-cell analysis from representative experiments (n=2). (Bottom) Representative images of the PLAs. Scale bar: 10 µm.

A

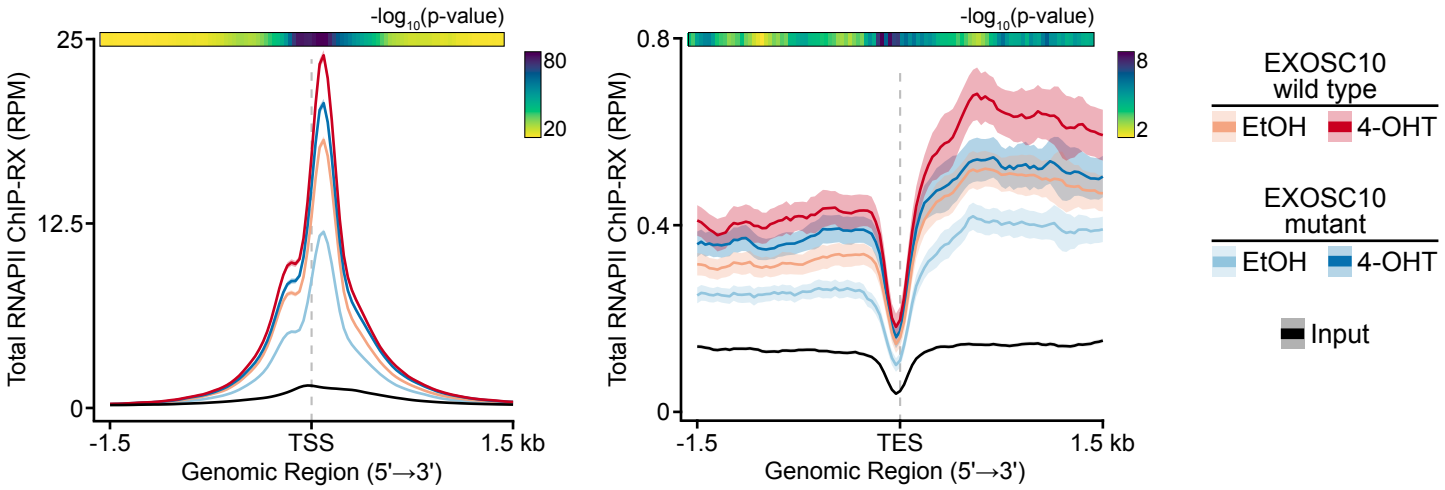

B

SH-EP-MYCNER RNA-seq

Ensembl gene ID	HGNC symbol	EtOH mean	4-OHT mean
ENSG00000187735	TCEA1	700	731
ENSG00000171703	TCEA2	126	92
ENSG00000204219	TCEA3	5	5

C

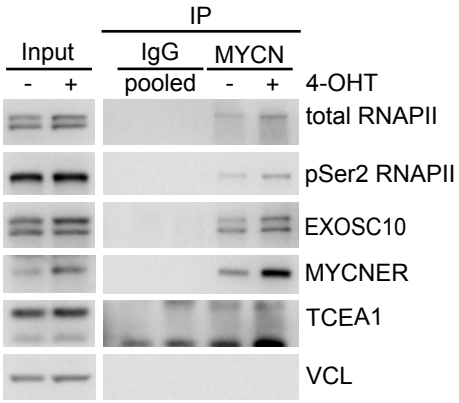

D

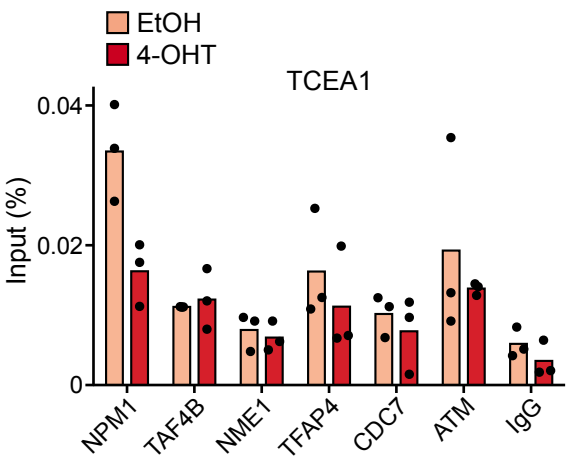

E

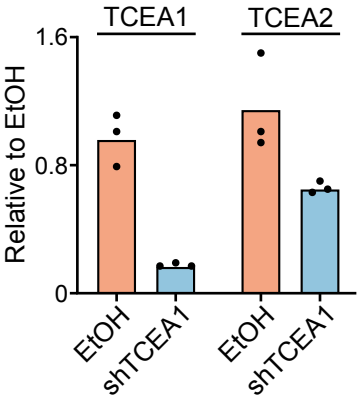

F

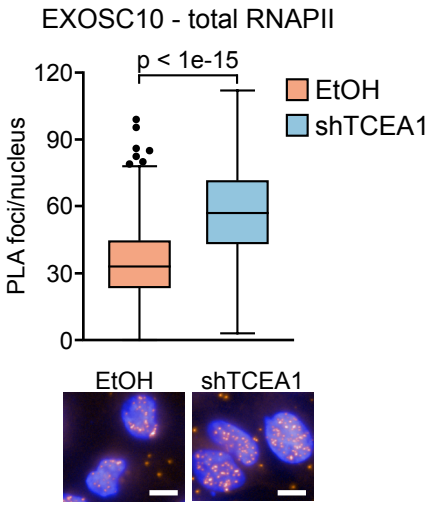

G

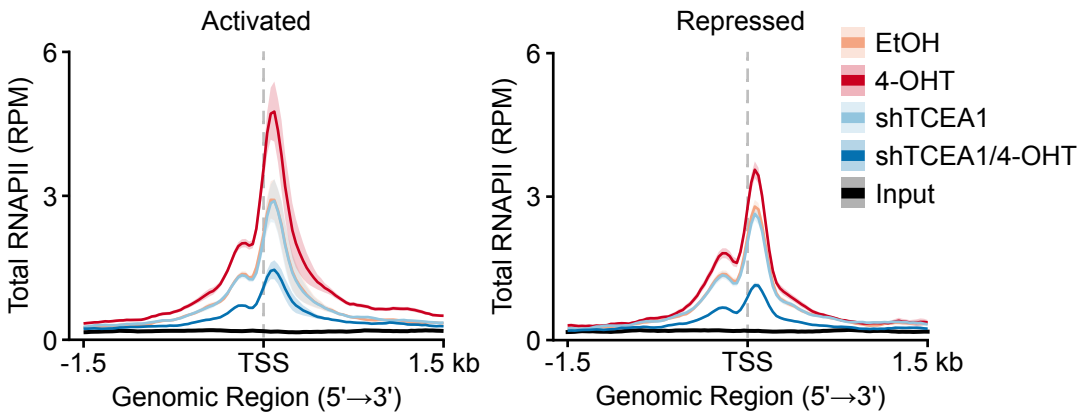

Figure S3. The RNA exosome has both MYCN-dependent and -independent effects on RNAPII. Related to Figure 3.

(A) Trimmed (1 %) mean read density of total RNAPII ChIP-RX data from SH-EP-MYCNER cells and SH-EP-MYCNER cells constitutively expressing a D313A/E315A inactive EXOSC10 mutant; for consistency, genes shorter than 8kb were excluded from the analysis. Cells were treated for 4 h with 4-OHT (200 nM), where indicated. Plots are centered around the TSS (left) or the TES (right) (n=1).

(B) RNA-seq data showing mean TCEA1-3 RNA levels in SH-EP-MYCNER cells treated for 3 h with 4-OHT (200 nM) (n=3). Data are taken from (Herold *et al.*, 2019).

(C) Immunoblot of MYCN IPs from SH-EP-MYCNER cells, treated for 4 h with 4-OHT (200 nM) where indicated (n=2).

(D) ChIP-qPCR showing TCEA1 binding to indicated loci in SH-EP-MYCNER cells. All primers used are TSS-proximal. Cells were treated for 4 h with 4-OHT (200 nM), where indicated. Dots indicate technical replicates (n=2).

(E) qPCR of TCEA1 and TCEA2 mRNA in SH-EP-MYCNER Dox-inducible TCEA1 shRNA cells after 72 h of Dox (shTCEA1) treatment. Dots indicate technical replicates (n=1).

(F) (Top) Quantification of nuclear PLA foci between EXOSC10 and total RNAPII in SH-EP-MYCNER Dox-inducible shTCEA1 cells. Cells were treated for 72 h with Dox (shTCEA1). Shown is single-cell analysis of a representative replicate (n=2). (Bottom) Representative images of quantified PLAs. Scale bar: 10 μm.

(G) Mean read density of total RNAPII ChIP-RX data from SH-EP-MYCNER Dox-inducible shTCEA1 cells for MYCN-activated (left) and -repressed (right) genes. Plots are centered around the TSS (n=2).

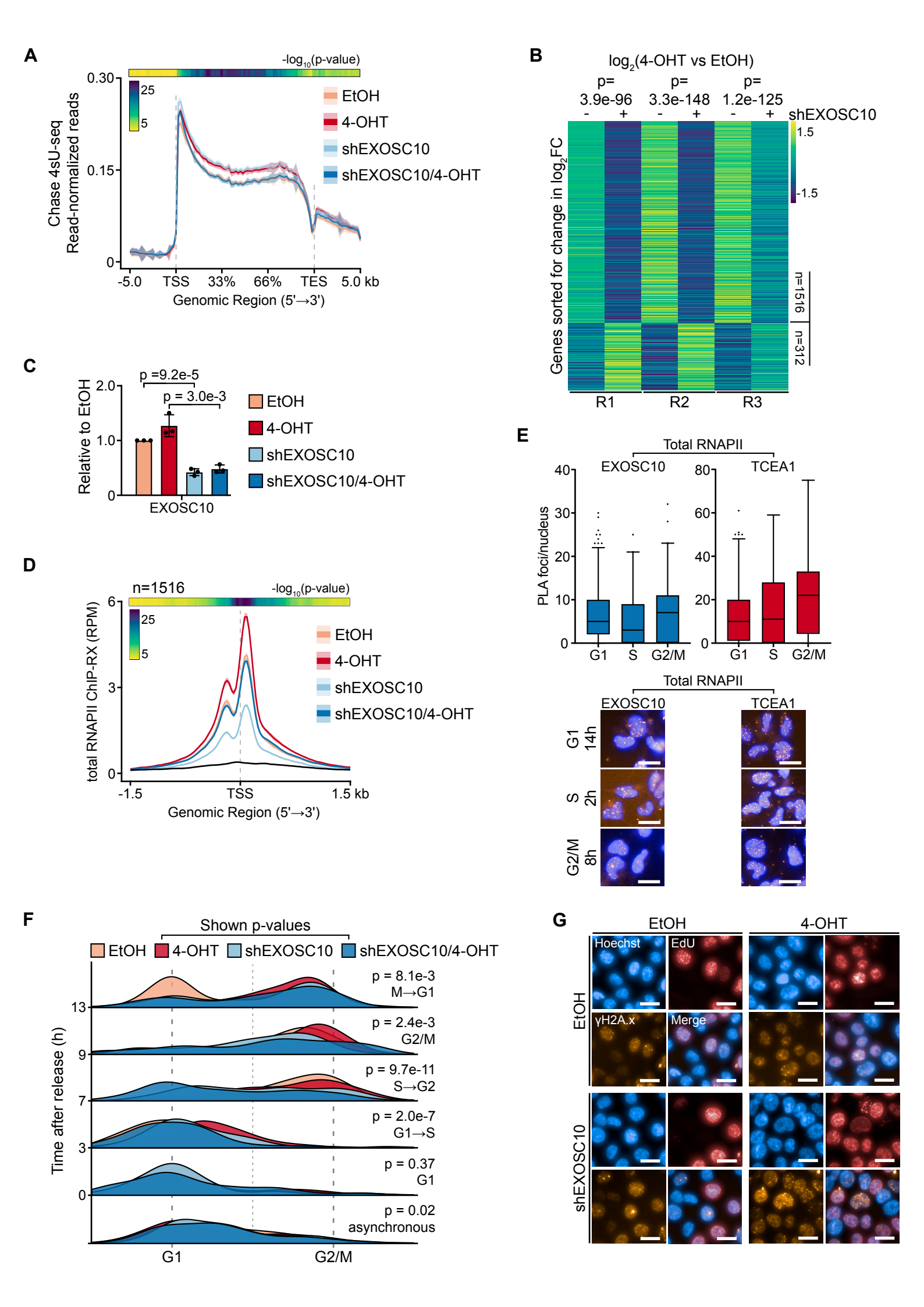
A
-log10(p-value)
Chase 4sU-seq
Read-normalized reads
EtOH
4-OHT
shEXOSC10
shEXOSC10/4-OHT
Genomic Region (5'→3')
B
log2(4-OHT vs EtOH)
p= 3.9e-96
p= 3.3e-148
p= 1.2e-125
shEXOSC10
Genes sorted for change in log2FC
n=1516
n=312
R1
R2
R3
C
p =9.2e-5
p = 3.0e-3
Relative to EtOH
EXOSC10
D
n=1516
total RNAPII ChIP-RX (RPM)
Genomic Region (5'→3')
E
Total RNAPII
EXOSC10
TCEA1
PLA foci/nucleus
G1
S
G2/M
F
Shown p-values
Time after release (h)
p = 8.1e-3
M→G1
p = 2.4e-3
G2/M
p = 9.7e-11
S→G2
p = 2.0e-7
G1→S
p = 0.37
G1
p = 0.02
asynchronous
G
EtOH
4-OHT
Hoechst
EdU
γH2A.x
Merge
shEXOSC10

Figure S4. The RNA exosome is required for MYCN-dependent transcription of cell cycle-regulated genes. Related to Figure 4.

(A) Trimmed (1 %) mean read metagene plot of 4sU-seq data in SH-EP-MYCNER cells expressing Dox-inducible EXOSC10 shRNA; genes longer than 8 kb are shown. Cells were treated with Dox for 72 h (shEXOSC10) and then for 4 h with 4-OHT (200 nM) where indicated, and 4sU (500 μM) was added during the last 20 min of culture. RNA was harvested after a 120 min chase. The heatmap above the plot indicates the p-value of the 4-OHT/EtOH difference in the presence of Dox, calculated from the density values of individual genes at each genomic location. Shown are merged replicates (n=3).

(B) Heatmap of Z-scores calculated from 4sU-labelled RNA levels in all three replicates and all conditions. Conditions are as in panel (A). After applying a bayesian p-value cut-off, the remaining 2166 genes were sorted for change in $\log_2$ fold-change (FC) between 4-OHT and EtOH (y-axis). P-values indicate whether the overall 4-OHT/EtOH ratios in 4sU-RNA levels are higher in the EtOH condition as compared to the shEXOSC10 condition.

(C) qPCR of EXOSC10 mRNA from samples used in 4sU-seq validation. Same conditions as panel (B).

(D) Trimmed (1 %) mean read density of total RNAPII ChIP-RX from SH-EP-MYCNER Dox-inducible shEXOSC10 cells centered around the TSS. Data are from the same experiment as in Figure 3C, but only the 1516 genes with a negative $\log_2$FC from 4sU-seq are shown (n=2).

(E) (Top) Quantification of nuclear PLA foci between total RNAPII and EXOSC10 or TCEA1 in IMR-5 cells synchronized by double thymidine block and fixed at indicated time points after release from block. Shown are representative single-cell analyses (n=3). (Bottom) Representative images from quantified PLAs. Scale bar: 20 μm.

(F) Density plots of DNA content in SH-EP-MYCNER Dox-inducible shEXOSC10 cells at indicated time points after double thymidine block synchronization and release. Cells were treated for 72 h with Dox (shEXOSC10) and 4-OHT, as indicated. DNA content is represented by Hoechst staining. Shown p-values compare difference in DNA content between the 4-OHT and shEXOSC10/4-OHT conditions in each time point (n=3).

(G) Representative immunofluorescence images from main Figures 4F,G. Scale bar: 20 μm.

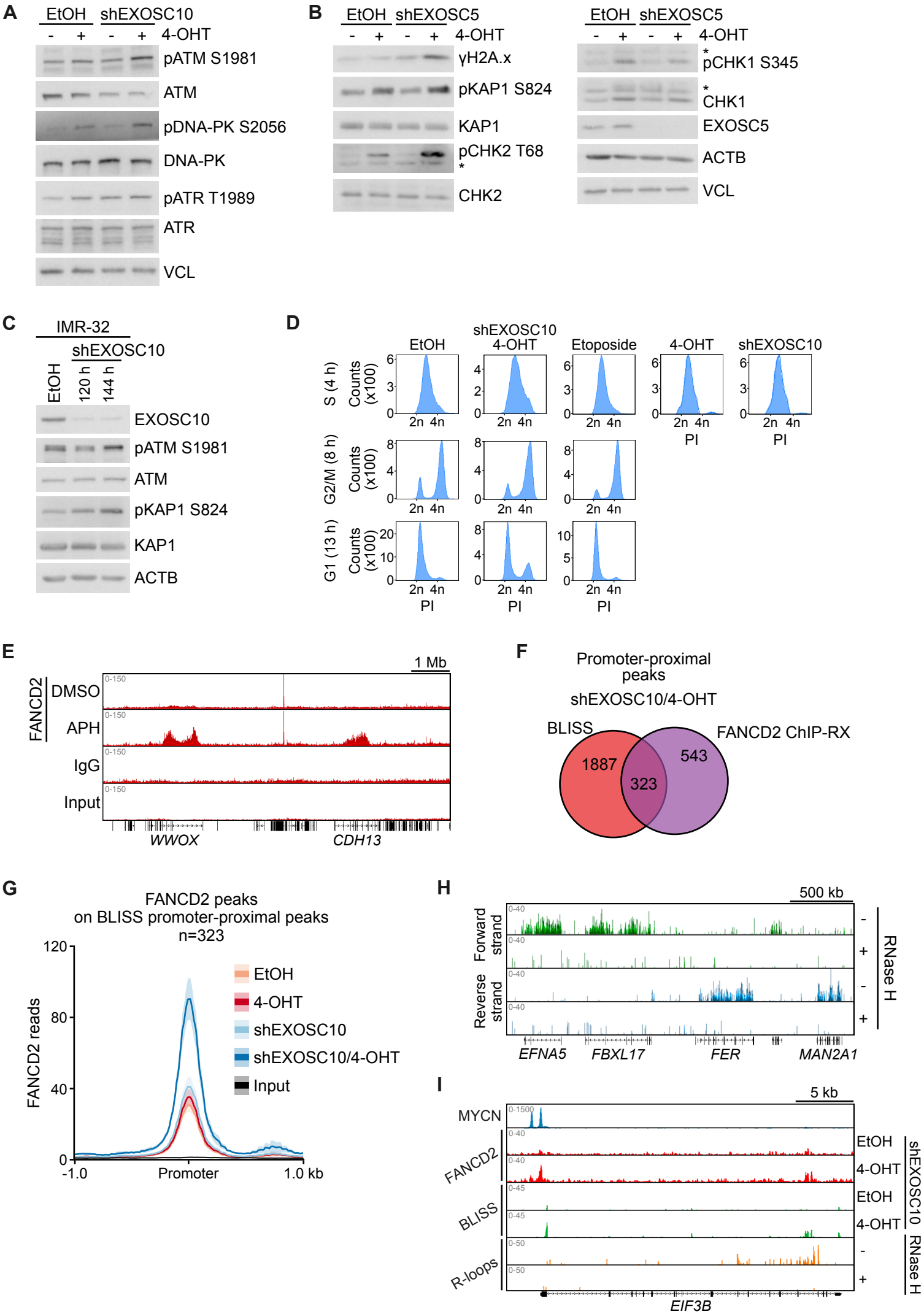
A
EtOH
shEXOSC10
- + - + 4-OHT
pATM S1981
ATM
pDNA-PK S2056
DNA-PK
pATR T1989
ATR
VCL
B
EtOH
shEXOSC5
- + - + 4-OHT
γH2A.x
pKAP1 S824
KAP1
pCHK2 T68
*
CHK2
EtOH
shEXOSC5
- + - + 4-OHT
*
pCHK1 S345
*
CHK1
EXOSC5
ACTB
VCL
C
IMR-32
shEXOSC10
EtOH
120 h
144 h
EXOSC10
pATM S1981
ATM
pKAP1 S824
KAP1
ACTB
D
EtOH
shEXOSC10 4-OHT
Etoposide
4-OHT
shEXOSC10
S (4 h)
G2/M (8 h)
G1 (13 h)
Counts (x100)
2n 4n
PI
E
1 Mb
FANCD2
DMSO
APH
IgG
Input
0-150
WWOX
CDH13
F
Promoter-proximal peaks
shEXOSC10/4-OHT
BLISS
FANCD2 ChIP-RX
1887
323
543
G
FANCD2 peaks
on BLISS promoter-proximal peaks
n=323
FANCD2 reads
120
80
40
0
-1.0
Promoter
1.0 kb
EtOH
4-OHT
shEXOSC10
shEXOSC10/4-OHT
Input
H
500 kb
Forward strand
Reverse strand
0-40
RNase H
EFNA5
FBXL17
FER
MAN2A1
I
5 kb
MYCN
0-1500
FANCD2
BLISS
R-loops
0-40
0-45
0-50
EtOH
4-OHT
shEXOSC10
RNase H
EIF3B

Figure S5. The RNA exosome prevents MYCN-driven double-strand break formation in S-phase. Related to Figure 5.

(A) Immunoblot of SH-EP-MYCNER Dox-inducible EXOSC10 shRNA cells. Cells were treated for 96 h with Dox (shEXOSC10) and 4-OHT, as indicated (n=2).

(B) Immunoblot of SH-EP-MYCNER Dox-inducible EXOSC5 shRNA cells. Cells were treated for 120 h with Dox (shEXOSC10) and 4-OHT, as indicated (n=2).

(C) Immunoblot of IMR-32 Dox-inducible shEXOSC10 cells. Cells were treated with Dox (shEXOSC10) for the indicated times (n=2).

(D) Propidium iodide FACS analysis of SH-EP-MYCNER Dox-inducible EXOSC10 shRNA cells synchronized with double-thymidine block and released at indicated time points. Where indicated, cells were treated for 48 h before and for 48 h during synchronization and released with Dox (shEXOSC10) and 4-OHT. Etoposide (25 μM) treatment took place for 2 h before harvest (n=1).

(E) Genome browser tracks from FANCD2 ChIP-RX showing chromatin binding of FANCD2 on indicated loci in SH-EP-MYCNER cells. Where indicated, cells were treated for 24 h with 400 nM aphidicolin (APH) (n=1).

(F) Venn diagram showing overlap of promoter-proximal BLISS and FANCD2 ChIP-RX peaks.

(G) Density plot of FANCD2 peaks that co-localize with BLISS TSS-proximal peaks in SH-EP-MYCNER Dox-inducible shEXOSC10 cells. For BLISS, cells were treated for 96 h with Dox (shEXOSC10) and 4-OHT, while for FANCD2 ChIP-RX cells were treated for 72 h with Dox and then for 4 h with 4-OHT (200 nM).

(H) Genome browser tracks showing R-loops on indicated loci on both DNA strands from DRIPc-seq carried out in *MYCN*-amplified IMR-5 cells. Samples were treated with RNase H, which specifically degrades R-loops, to filter out unspecific signals, as indicated.

(I) Genome browser tracks from MYCN and FANCD2 ChIP-RX, BLISS and DRIPc-seq at the *EIF3B* locus.

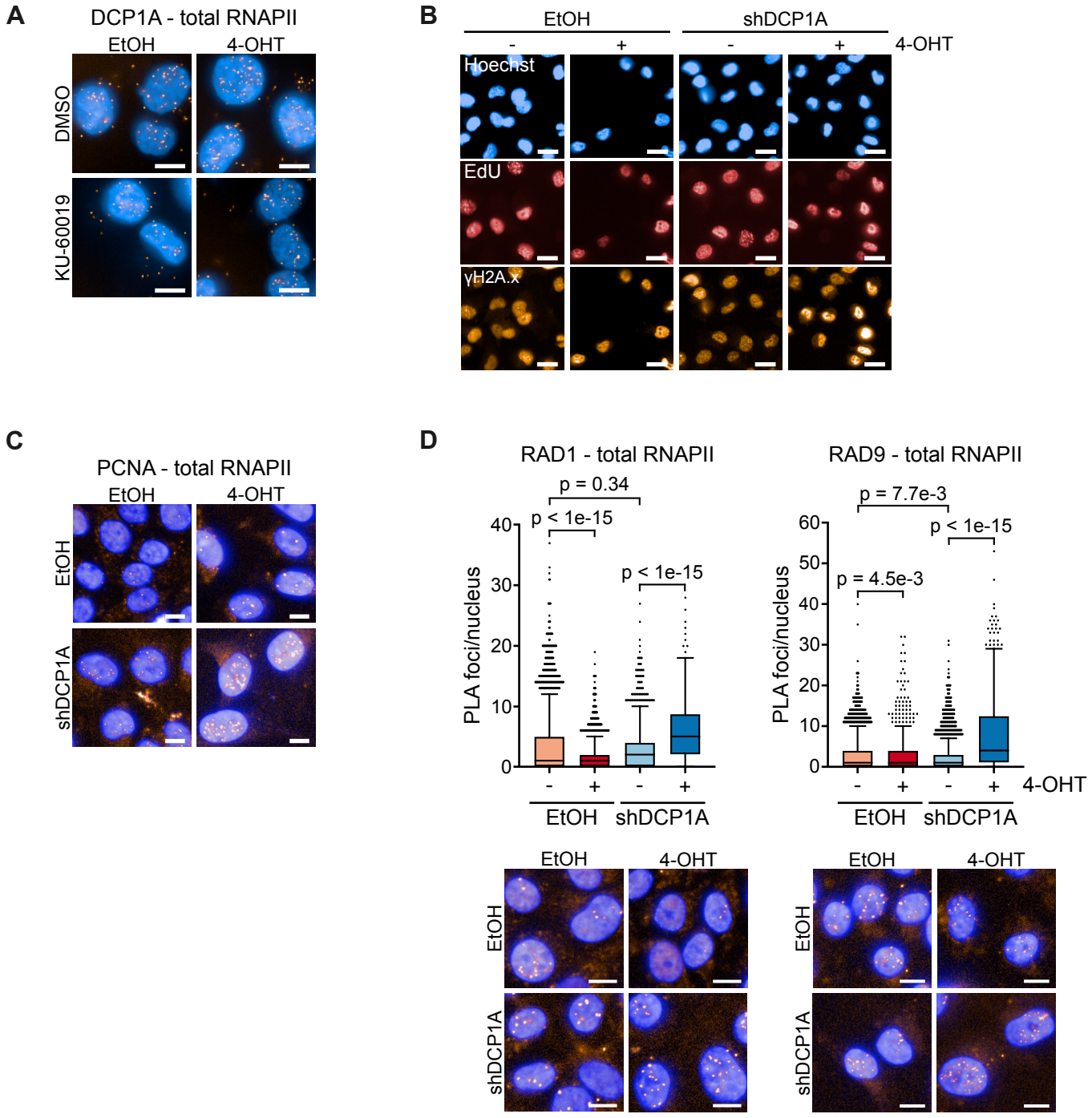

Figure S6. mRNA decapping prevents MYCN-dependent transcription-replication conflicts. Related to Figures 6 and 7.

(A) Representative images of DCP1A-total RNAPII PLAs shown in Figure 6E. Scale bar: 10 μm.

(B) Representative immunofluorescence images shown in Figures 7B and 7C. Scale bar: 20 μm.

(C) Representative images of PCNA-total RNAPII PLAs shown in Figure 7F. Scale bar: 10 μm.

(D) (Top) Quantification of nuclear PLA foci between total RNAPII and RAD1 or RAD9 in SH-EP-MYCNER Dox-inducible shDCP1A cells. Cells were treated for 144 h with Dox (shDCP1A) and 4-OHT, as indicated. Shown are single cell analyses from representative experiments (n=3 for RAD1, n=2 for RAD9). (Bottom) Representative images of PLAs. Scale bar: 10 μm.